

Connecting the Dots: Numerical Randomized Hamiltonian Monte Carlo with State-Dependent Event Rates

Tore Selland Kleppe*

February 1, 2022

Abstract

Numerical Generalized Randomized Hamiltonian Monte Carlo is introduced, as a robust, easy to use and computationally fast alternative to conventional Markov chain Monte Carlo methods for continuous target distributions. A wide class of piecewise deterministic Markov processes generalizing Randomized HMC (Bou-Rabee and Sanz-Serna, 2017) by allowing for state-dependent event rates is defined. Under very mild restrictions, such processes will have the desired target distribution as an invariant distribution. Secondly, the numerical implementation of such processes, based on adaptive numerical integration of second order ordinary differential equations (ODEs) is considered. The numerical implementation yields an approximate, yet highly robust algorithm that, unlike conventional Hamiltonian Monte Carlo, enables the exploitation of the complete Hamiltonian trajectories (hence the title). The proposed algorithm may yield large speedups and improvements in stability relative to relevant benchmarks, while incurring numerical biases that are negligible relative to the overall Monte Carlo errors. Granted access to a high-quality ODE code, the proposed methodology is both easy to implement and use, even for highly challenging and high-dimensional target distributions.

Keywords: Hamiltonian Monte Carlo, MCMC, Piecewise deterministic processes, Runge-Kutta-Nystrom

1 Introduction

By now, Markov chain Monte Carlo (MCMC) methods and their widespread application in Bayesian statistics need no further introduction (see e.g. Gelman et al., 2014; Robert and Casella, 2004). In this paper, Generalized Randomized Hamiltonian Monte Carlo (GRHMC), a wide class of continuous time Markov processes with a pre-selected stationary distribution is constructed. Further, Numerical GRHMC (NGRHMC),

*Department of Mathematics and Physics, University of Stavanger, 4036 Stavanger, Norway. Email: tore.kleppe@uis.no

the practical implementation of GRHMC processes is suggested as a robust and easy to use general purpose class of algorithms for solving problems otherwise handled using MCMC methods for continuous state spaces.

The paper makes several contributions. GRHMC processes, a wide class of piecewise deterministic Markov processes (PDMP) (see e.g. Davis, 1993; Fearnhead et al., 2018; Vanetti et al., 2018, and references therein) with target distribution-preserving Hamiltonian deterministic dynamics are defined. GRHMC processes generalizes Randomized HMC (Bou-Rabee and Sanz-Serna, 2017) by admitting state-dependent event-rates, while still retaining arbitrary pre-specified stationary distributions. The highly flexible specification of event rates leaves substantial room to construct processes that are more optimized towards MCMC applications. A further benefit of using conserving Hamiltonian deterministic dynamics is that GRHMC processes are likely to scale well to high-dimensional problems (see e.g., Bou-Rabee and Eberle, 2020 where dimension-free convergence bounds are obtained for the Anderson Thermostat, which generalizes RHMC).

Secondly, it is proposed to use adaptive numerical methods for second order ordinary differential equations (ODEs) (see e.g. Hairer et al., 1993) to approximate a selected GRHMC process to arbitrary precision, leading to NGRHMC. In common implementations of Hamiltonian Monte Carlo, errors introduced by fixed time step (i.e., non-adaptive) symplectic/time-reversible integrators are exactly corrected using accept/reject steps. Here, biases relative to the (on target, but generally intractable) GRHMC process stemming from the numerical integration of ODEs are not explicitly corrected for, but rather kept under control by choosing the ODE integrator precision sufficiently high. Numerical experiments indicate that even for rather lax integrator precision, biases incurred by the numerical integration of ODEs are imperceptible relative to the overall Monte Carlo variation stemming from using MCMC-like methods.

By allowing for such small biases, one may leverage high quality adaptive ODE integration codes, making the proposed method both easy to implement and requiring minimal expertise by the user. The system of ODEs may be augmented beyond Hamilton's equations so that sampling of event times under non-trivial event rates (without specifying model-specific bounds on the event rates (Fearnhead et al., 2018)) and computing averages over continuous time trajectories are done within ODE solver. This practice of augmenting the ODE system ensures that the precision of the overall algorithm (including the simulation of event times and computation of moments) relative to the underlying GRHMC process is controlled by a single error control mechanism and only a few easily interpretable tuning parameters. Automatic tuning methodology of the parameters in underlying GRHMC process, again leveraging aspects of the adaptive ODE integration code, is also proposed.

Thirdly, it is demonstrated that certain moments of the target distribution may be estimated extremely efficiently by exploiting the between events Hamiltonian dynamics (and hence the name of the paper). Such improved efficiency occur when the temporal averages of the position coordinate of the Hamiltonian trajec-

tories (without momentum refreshes) coincide with the corresponding means under the target distributions. Such effects occurs e.g., when estimating the mean under Gaussian target distributions, but is by no means restricted to this situation. Exploitation of any such effects is straight forward when the theoretical processes are approximated using ODE solvers as proposed.

Finally, it is demonstrated that even rudimentary versions of NGRHMC have competitive performance compared to commonly used (fixed time step) symplectic/time-reversible methods for target distributions where the latter methods work well. Furthermore, it is demonstrated that adaptive nature of the integrators employed here resolves the slow exploration associated with fixed step size HMC-MCMC chains for target distributions exhibiting certain types of non-linearities.

This paper contains only initial steps towards understanding and exploiting the full potential of GRHMC processes and their numerical implementation and should be read as an invitation to further work. On the theoretical side, understanding the ergodicity of GRHMC processes beyond RHMC, bounding the biases stemming from numerical integration and understanding scaling in high dimensions would be natural next steps. Better exploiting the possibilities afforded by the highly flexible state-dependent event rates constitutes another major avenue for further work. Throughout the text, further suggestions for continued research in several other regards are also pointed out.

1.1 Relation to other work

Continuous time Markov processes involving Hamiltonian dynamics subject to random updates of velocities at random times are by no means new. In the molecular simulation literature, the Anderson Thermostat (AT) (Andersen, 1980) involves Hamiltonian dynamics with updating of the momentum of randomly chosen particles according to Boltzmann-Gibbs distribution marginals. RHMC may be seen as a special case of the AT with only one particle (Bou-Rabee and Eberle, 2020). Uncorrected numerical implementations of the AT, involving fixed time step reversible integrators may be found in several molecular simulation packages such as GROMACS (Abraham et al., 2015).

The theoretical properties of the RHMC (with constant event rate and exact Hamiltonian dynamics) and AT have been extensively studied: Bou-Rabee and Sanz-Serna (2017) develop geometric ergodicity of RHMC under mild assumptions. Further, E and Li (2008); Li (2007) develop ergodicity for both continuous time AT and its time-discretization under different assumptions, and Bou-Rabee and Eberle (2020) consider the convergence of AT in Wasserstein distance. Lu and Wang (2020) study RHMC under the hypocoercivity framework. As described by Bou-Rabee and Sanz-Serna (2017), there is also an interesting and fundamental connection between RHMC and second order Langevin dynamics (see e.g. Cheng et al., 2018, and references

therein) in that the same stochastic Lyapunov function may be used to prove geometric ergodicity of both types of processes.

Recently, PDMPs (see e.g. Davis, 1993; Fearnhead et al., 2018; Vanetti et al., 2018, and references therein) have received substantial interest as time-irreversible alternatives to conventional MCMC methods. Most proposed PDMP-based alternatives to MCMC, such as the Bouncy Particle Sampler (Bouchard-Côté et al., 2018) and the Zig-Zag process (Bierkens et al., 2019) rely on linear deterministic dynamics. Another PDMP-based sampling algorithm; The Boomerang Sampler (BS) (Bierkens et al., 2020) uses the explicitly solvable Hamiltonian deterministic dynamics associated with Gaussian approximation to the target. The BS was found to outperform the mentioned linear dynamics PDMPs. AT, RHMC along with GRHMC are also PDMPs based on Hamiltonian deterministic dynamics, but unlike the BS, the involved deterministic dynamics preserves exactly the target distribution, hence affording GRHMC substantial flexibility with respect to the selection of event rates. Interestingly, Deligiannidis et al. (2018) shows that the RHMC process is a scaling limit of the Bouncy Particle Sampler (Bouchard-Côté et al., 2018). RHMC processes (i.e. with exact Hamiltonian dynamics and constant event rates) are also mentioned in the context of PDMPs by Vanetti et al. (2018, footnote 3), but no details are provided on how to implement such an algorithm are provided.

Inter-event time sampling for PDMPs based on numerical integration and root-finding (and thereby bypassing the need for global bounds on the event rate as is also done in this paper) is considered by Cotter et al. (2020). However, their approach is based on the linear Zig-Zag dynamics and uses other numerical techniques to obtain integrated event rates. HMC-MCMC based on exact Hamiltonian dynamics is considered by Pakman and Paninski (2014), but their approach is restricted to truncated Gaussian distributions where such dynamics may be found on closed form. Theoretical work for HMC-MCMC assuming exact target-preserving Hamiltonian dynamics may be found in e.g., Mangoubi and Smith (2017); Chen and Vempala (2019). Nishimura and Dunson (2020) consider recycling the intermediate integrator-steps in HMC-MCMC in a manner related to the temporal averages considered here, and also find substantial improvements in simulation efficiency in numerical experiments.

Unadjusted (and therefore generally biased) numerical approximations to intractable theoretical processes for simulation purposes have received much attention, with the widely used stochastic gradient Langevin dynamics (Welling and Teh, 2011) being such an example. In particular, both first- and second order Langevin dynamics, along with their multiple integration step counterpart, generalized HMC (Horowitz, 1991), have been implemented in unadjusted manners (see e.g. Leimkuhler and Matthews, 2015, for an overview). In addition, several theoretical papers consider unadjusted HMC-MCMC algorithms, see e.g., Mangoubi and Smith (2019), Bou-Rabee and Schuh (2020) and Bou-Rabee and Eberle (2021). In this strand of literature,

also so-called collocation methods (which are closely related to certain Runge Kutta methods (Hairer et al., 1993)) are applied by Lee et al. (2018) for solving Hamilton’s equations, but their approach is again based on (discrete time-)HMC-MCMC and does not appear to leverage modern numerical ODE techniques. Finally, the present use of adaptive step size techniques has similarities to Kleppe (2016), but the latter algorithm is based on Langevin processes and involves a Metropolis-Hastings adjustment step.

The reminder of this paper is laid out as follows: Section 2 provides background and fixes notation. GRHMC processes are defined and discussed in Section 3. The practical numerical implementation of such processes is discussed in Section 4. Numerical experiments and illustrations, along with benchmarks against Stan are given in Sections 5 and 6. Finally, Section 7 provides discussion. The complete set of source code underlying this paper is available at <https://github.com/torekleppe/PDPHMCpaperCode>.

2 Background

This section provides some background and fixes notation for subsequent use. Throughout this paper, a target distribution with density $\pi(\mathbf{q})$, $\mathbf{q} \in \Omega \subseteq \mathbb{R}^d$ with an associated density kernel $\tilde{\pi}(\mathbf{q})$ which can be evaluated point-wise. The gradient/Jacobian operator of a function with respect to some variable, say \mathbf{x} , is denoted by $\nabla_{\mathbf{x}}$. Time-derivatives are denoted using the conventional dot-notation, i.e. $\dot{f}(\tau) = \frac{d}{d\tau}f(\tau)$, $\ddot{f}(\tau) = \frac{d^2}{d\tau^2}f(\tau)$ for some function $f(\tau)$ evolving over time τ .

In the reminder of this section, Hamiltonian mechanics, HMC and PDMPs are briefly reviewed in order to fix notation and provide the required background. The reader is referred to Goldstein et al. (2002); Leimkuhler and Reich (2004) and Neal (2010); Bou-Rabee and Sanz-Serna (2018) for more detailed expositions of Hamiltonian mechanics and HMC. Davis (1984, 1993) for consider PDMPs in general and Fearnhead et al. (2018); Vanetti et al. (2018) give details for Monte Carlo applications of PDMPs.

2.1 Elements of Hamiltonian mechanics

Hamiltonian Monte Carlo methods rely on specifying a physical system and use the dynamics of this system to propose transitions. The state $\mathbf{z} = [\mathbf{q}^T, \mathbf{p}^T]^T \in \mathbb{R}^{2d}$ of the system is characterized by a position coordinate $\mathbf{q} \in \mathbb{R}^d$ and a momentum coordinate $\mathbf{p} \in \mathbb{R}^d$. The system itself is conventionally specified in terms of the Hamiltonian $\mathcal{H}(\mathbf{z}) = \mathcal{H}(\mathbf{q}, \mathbf{p})$ which gives the total energy of the system for a given state \mathbf{z} . Throughout this work, physical systems with Hamiltonian given as

$$\mathcal{H}(\mathbf{q}, \mathbf{p}) = -\log \tilde{\pi}(\mathbf{q}) + \frac{1}{2}\mathbf{p}^T \mathbf{M}^{-1}\mathbf{p}, \tag{1}$$

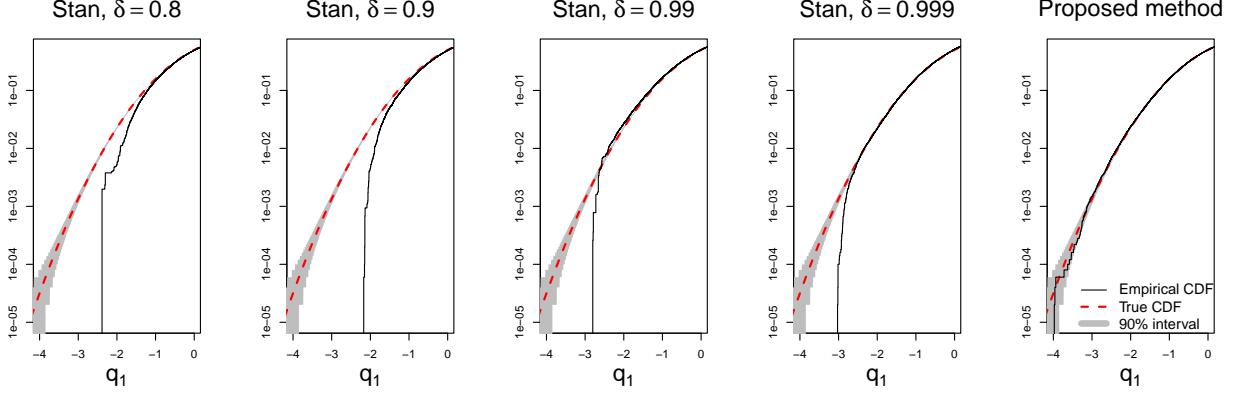


Figure 1: Empirical cumulative distribution functions (CDFs) associated with MCMC output for the standard Gaussian \mathbf{q}_1 -marginal under the “funnel”-model $\mathbf{q}_1 \sim N(0, 1)$, $\mathbf{q}_2|\mathbf{q}_1 \sim N(0, \exp(3\mathbf{q}_1))$. For visual clarity, only the left half of the distributions are presented. Further details on this experiment can be found in Section 5.1. Each case is based on 5000 samples from each of 10 independent replica. The black solid lines are the empirical CDFs, whereas the red dashed lines are the true CDFs. The shaded gray region would cover 90% of empirical CDFs based on 50000 iid $N(0, 1)$ samples point-wise. The four left-most panels are based on Stan output with different values of the accept rate target δ . In practice, higher values of δ corresponds to smaller integrator step sizes and more integrator steps per produced sample. The right-most panel shows output for the proposed methodology using constant event rates. For both Stan and the proposed methodology, an identity mass matrix was employed.

are considered. Here $\mathbf{M} \in \mathbb{R}^{d \times d}$ is a symmetric, positive definite (SPD) mass matrix which is otherwise specified freely. The time-evolution of the system is given by Hamilton’s equations $\dot{\mathbf{q}}(\tau) = \nabla_{\mathbf{p}} \mathcal{H}(\mathbf{q}(\tau), \mathbf{p}(\tau))$, $\dot{\mathbf{p}}(\tau) = -\nabla_{\mathbf{q}} \mathcal{H}(\mathbf{q}(\tau), \mathbf{p}(\tau))$, which for Hamiltonian (1) reduces to:

$$\dot{\mathbf{z}}(\tau) = \begin{bmatrix} \dot{\mathbf{q}}(\tau) \\ \dot{\mathbf{p}}(\tau) \end{bmatrix} = \begin{bmatrix} \mathbf{M}^{-1} \mathbf{p}(\tau) \\ \nabla_{\mathbf{q}} \log \tilde{\pi}(\mathbf{q}(\tau)) \end{bmatrix} \quad (2)$$

The flow associated with (2) is denoted by $\varphi_\tau(\cdot)$, and is defined so that $\mathbf{z}(\tau + s) = \varphi_s(\mathbf{z}(\tau))$ solves (2) for any scalar time increment s , initial time τ and initial configuration $\mathbf{z}(\tau)$. The flow can be shown to be

- Energy preserving, i.e. $\frac{\partial}{\partial \tau} \mathcal{H}(\varphi_\tau(\mathbf{z})) = 0$ for all admissible \mathbf{z} ,
- Volume preserving, i.e. $|\nabla_{\mathbf{z}} \varphi_\tau(\mathbf{z})| = 1$ for each fixed τ and all admissible \mathbf{z} ,
- Time reversible, which in the present context is most conveniently formulated via that $\mathbf{T}_\tau = \mathbf{R} \circ \varphi_\tau$ is an involution so that $\mathbf{T}_\tau \circ \mathbf{T}_\tau$ is the identity operator. The momentum flip operator $\mathbf{R} = \text{diag}(\mathbf{I}_d, -\mathbf{I}_d)$ effectively reverses time.

2.2 Hamiltonian Monte Carlo

In the context of statistical computing, Hamiltonian dynamics has attracted much attention the last decade. This interest is rooted in that the flow φ_τ of (2) (and associated involution \mathbf{T}_τ) exactly preserves the Boltzmann-Gibbs (BG) distribution

$$\rho(\mathbf{z}) = \rho(\mathbf{q}, \mathbf{p}) = \pi(\mathbf{q})\mathcal{N}(\mathbf{p}|\mathbf{0}_d, \mathbf{M}) \propto \exp(-\mathcal{H}(\mathbf{q}, \mathbf{p})), \quad (3)$$

associated with \mathcal{H} . I.e., for each fixed time increment τ , $\varphi_\tau(\mathbf{z}) \sim \rho$ whenever $\mathbf{z} \sim \rho$. It is seen that the target distribution is the \mathbf{q} -marginal of the BG distribution. Thus, a hypothetical MCMC algorithm targeting (3), and producing samples $\mathbf{z}_{(i)} = (\mathbf{q}_{(i)}^T, \mathbf{p}_{(i)}^T)^T$, would involve the BG distribution-preserving steps:

- Sample $\mathbf{p}_* \sim N(\phi\mathbf{p}_{(i-1)}, \sqrt{1-\phi^2}\mathbf{M})$ for some $\phi \in (-1, 1)$ and set $\mathbf{z}_* = (\mathbf{q}_{(i-1)}^T, \mathbf{p}_*^T)^T$.
- For some suitable time increment s , $\mathbf{z}_{(i)} = \varphi_s(\mathbf{z}_*)$.

Subsequently, the momentum samples, $\mathbf{p}_{(i)}$, may be discarded to obtain samples targeting $\pi(\mathbf{q})$ only. Randomized durations s may be introduced in order to avoid periodicities or near-periodicities in the underlying dynamics, and may result in faster convergence (Mackenzie, 1989; Cances et al., 2007; Bou-Rabee and Sanz-Serna, 2017, 2018). Alternatively, more sophisticated algorithms can be used to avoid u-turns (Hoffman and Gelman, 2014).

For all but the most analytically tractable target distributions, the flow associated with Hamilton's equations is not available in closed form, and hence it must be integrated numerically for the practical implementation of the above MCMC sampler. Provided a time-reversible integrator is employed for this task, the numerical error incurred in the second step of the above MCMC algorithm can be exactly corrected using an accept/reject step (Fang et al., 2014), but the accept probability may be computationally demanding. If the employed integrator is also volume preserving (i.e. symplectic) (see e.g. Leimkuhler and Reich, 2004), the accept-probability depends only on the values of the Hamiltonian before and after the integration. This simplification has led to the widespread application of the symplectic leap-frog (or Størmer-Verlet) integrator in HMC implementations such as e.g., Stan (Stan Development Team, 2017).

Requiring the integrator to be time reversible and symplectic imposes rather strict restrictions on the integration process. In particular the application of adaptive (time-)step sizes, which is an integral part of any modern general purpose numerical ODE code, is at best difficult to implement (see Leimkuhler and Reich, 2004, Chapter 9 for discussion of this problem) while maintaining time-reversible and symplectic properties.

Figure 1 illustrates the effect of using fixed step sizes for the funnel-type distribution $q_1 \sim N(0, 1)$,

$q_2|q_1 \sim N(0, \exp(3q_1))$ (further details on this experiment can be found in Section 5.1). In the four left panels, empirical cumulative distribution functions (CDFs) calculated from MCMC output using the fixed step size integrator in Stan are depicted for various accept rate targets δ which has a default value of 0.8. In practice, higher values of δ correspond to higher fidelity integration with smaller integrator step sizes and more integrator steps per produced sample. It is seen that even with very small step sizes, Stan fails to properly represent the left-hand tail of q_1 (which imply a very small scale in the q_2). In the $\delta = 0.999$ case, the smallest produced sample out 50000 is ≈ -3.026 . In an iid $N(0, 1)$ sample of this size, one would expect around 62 samples smaller than this value.

Also included in Figure 1 are results from a variant of the proposed methodology (see Section 5.1 for details), which is based on adaptive numerical integrators. The method shows no such pathologies, and in particular the number of samples below the smallest $\delta = 0.999$ Stan sample was 70.

2.3 Piecewise deterministic Markov processes

Recently, continuous time piecewise deterministic Markov processes (PDMP) (see e.g. Davis, 1984, 1993) have been considered as alternatives to discrete time Markov chains produced by conventional MCMC methods. PDMPs may be employed for simulating dependent samples, or more generally continuous time trajectories with a given marginal probability distribution (see Fearnhead et al., 2018, and references therein). As the name indicates, PDMPs follow a deterministic trajectory between events occurring at stochastic times. At events, the state is updated in a stochastic manner.

Following Fearnhead et al. (2018), a PDMP, say $\mathcal{Z}(t) \in \mathbb{R}^D$, $t \in [0, \infty)$, is specified in terms of three components (Φ, λ, Q) :

- Deterministic dynamics on *time intervals where events do not occur*, specified in terms of a set of ODEs: $\dot{\mathcal{Z}}(t) = \Phi(\mathcal{Z}(t))$.
- A non-negative event rate $\lambda(\mathcal{Z}(t))$, depending only on the current state of the process, so that the probability of an event between times t and $t + r$, $r \geq 0$ is $\lambda(\mathcal{Z}(t))r + o(r)$ for small r .
- Finally, a “transition distribution at events” $Q(\cdot|\mathcal{Z}(t-))$. Suppose an event occurs at time t , and $\mathcal{Z}(t-)$ is the state immediately before time t . Then the $\mathcal{Z}(t)$ will be drawn randomly with density $Q(\cdot|\mathcal{Z}(t-))$.

Let Ξ_s be the flow associated with Φ . In order to simulate from a PDMP, suppose first that $\mathcal{Z}(0)$ has been set to some value, and that t is initially set to zero. Then the following three steps are repeated until $t > T$ where T is the desired length of the PDMP trajectory:

- Simulate a new $u \sim \text{Exp}(1)$ and subsequently compute the time-increment until next event v , which obtains as the solution in v to

$$\Lambda(v; \mathcal{Z}(t)) = u, \text{ where } \Lambda(v; \mathbf{z}) = \int_0^v \lambda(\Xi_s(\mathcal{Z}(t))) ds. \quad (4)$$

- Set $\mathcal{Z}(t+s) = \Xi_s(\mathcal{Z}(t))$ for all $s \in [0, v)$, and $\mathcal{Z}^* = \Xi_v(\mathcal{Z}(t))$.
- Set $t \leftarrow t + v$ and simulate $\mathcal{Z}(t) \sim Q(\cdot | \mathcal{Z}^*)$.

An invariant distribution of the process $\mathcal{Z}(t)$, say $p(\mathbf{z})$, will satisfy the time-invariant Fokker-Planck/Kolmogorov forward equation (Fearnhead et al., 2018)

$$\sum_{i=1}^D \frac{\partial}{\partial z_i} [\Phi_i(\mathbf{z}) p(\mathbf{z})] = \int p(\mathbf{z}') \lambda(\mathbf{z}') Q(\mathbf{z} | \mathbf{z}') d\mathbf{z}' - p(\mathbf{z}) \lambda(\mathbf{z}), \quad (5)$$

for all admissible states \mathbf{z} . For continuous time Monte Carlo applications, one therefore seeks combinations of (Φ, λ, Q) so that the desired target distribution is an invariant distribution $p(\mathbf{z})$.

Provided such a combination has been found, discrete time Markovian samples

$$\mathbf{z}_{(i)} = \mathcal{Z}(\Delta i), \text{ for some sample spacing } \Delta > 0, \quad (6)$$

may be used in the same manner as regular MCMC samples for characterizing the invariant distribution. In addition, by letting the sample spacing $\Delta \rightarrow 0$, moments under the invariant distribution may also be obtained by utilizing the complete trajectory of the PDMP, i.e.

$$\frac{1}{T} \int_0^T g(\mathcal{Z}(t)) dt \xrightarrow{T \rightarrow \infty} \int g(\mathbf{z}) p(\mathbf{z}) d\mathbf{z} \text{ almost surely,} \quad (7)$$

for some function g .

In most current implementations of PDMPs, λ depends on $\nabla_{\mathbf{q}} \log \tilde{\pi}(\mathbf{q})$ and hence $\Lambda(v; \mathbf{z})$ cannot be evaluated analytically, complicating the simulation of between event times, v , according to (4). The between event times are most commonly resolved using thinning (see e.g. Fearnhead et al., 2018, Section 2.1), which in turn necessitates selecting an upper bound on λ specific to the target distribution in question. The tightness of the bound substantially influences the computational cost of the resulting method. Similar to the present work, Cotter et al. 2020 bypasses the need for such bounds by approximating $\Lambda(v; \mathbf{z})$ using numerical integration and solve (4) using numerical root finding, thereby obtaining a PDMP that is slightly biased relative to the target distribution.

3 Generalized randomized HMC processes

In this section, theoretical PDMPs with (appropriately chosen) Hamiltonian dynamics (2) between events are considered. These processes will be referred to a generalized randomized HMC processes (GRHMC), and it shown that for a large class of combinations of (λ, Q) , GRHMC processes will have the BG distribution (3) as a stationary distribution. In practice, the Hamiltonian flow is implemented using high precision adaptive numerical methods (to be discussed in Section 4.1 and referred to as Numerical GRHMC), to obtain a robust and accurate, but nevertheless *approximate* versions of these PDMPs.

3.1 GRHMC as PDMPs

The GRHMC process targeting $\rho(\mathbf{z})$ is constructed within the PDMP framework of Section 2.3 as follows; set $D = 2d$, $\mathbf{z} = [\mathbf{q}^T, \mathbf{p}^T]^T$ and,

- The deterministic dynamics are Hamiltonian, namely

$$\Phi(\mathbf{z}) = \begin{bmatrix} \mathbf{M}^{-1}\mathbf{p} \\ \nabla_{\mathbf{q}} \log \tilde{\pi}(\mathbf{q}) \end{bmatrix}, \text{ and hence } \Xi_{\tau} = \varphi_{\tau}. \quad (8)$$

- A general *state-dependent* event rate $\lambda(\mathbf{z}) = \lambda(\mathbf{q}, \mathbf{p}) > 0$ subject only to the restriction that $C(\mathbf{q}) = \int \lambda(\mathbf{q}, \mathbf{p}) \mathcal{N}(\mathbf{p}|\mathbf{0}_d, \mathbf{M}) d\mathbf{p} < \infty$ (for all admissible \mathbf{q}) is assumed.
- The “transition distribution at events” is given in terms of the density

$$Q(\mathbf{z}|\mathbf{z}') = \delta(\mathbf{q} - \mathbf{q}') K_{\mathbf{q}'}(\mathbf{p}|\mathbf{p}'), \quad (9)$$

where $K_{\mathbf{q}}(\mathbf{p}|\mathbf{p}')$ is a Markov kernel density which leaves $v_{\mathbf{q}}(\mathbf{p}) = \lambda(\mathbf{q}, \mathbf{p}) \mathcal{N}(\mathbf{p}|\mathbf{0}_d, \mathbf{M}) [C(\mathbf{q})]^{-1}$ invariant for all fixed \mathbf{q} , where and $\delta(\cdot)$ is the Dirac delta function centered in $\mathbf{0}$.

From now on, $\mathcal{Q}(t)$ and $\mathcal{P}(t)$ are used for position- and momentum sub-vectors of $\mathcal{Z}(t)$ respectively, i.e. $\mathcal{Z}(t) = [\mathcal{Q}(t)^T, \mathcal{P}(t)^T]^T$, $t \in [0, T]$.

3.2 Stationary distribution

Proposition 1: *The above introduced GRHMC processes admit $\rho(\mathbf{z})$ as a stationary distribution.*

Proposition 1 is proved by showing that both sides of the steady state Fokker-Planck equation (5) with $p(\mathbf{z}) = \rho(\mathbf{z})$ are zero for a GRHMC process. As shown in Appendix A.1, for BG-preserving Hamiltonian

dynamics (8) between events, the left-hand side of the Fokker-Planck equation (5) vanishes, i.e.

$$\sum_{i=1}^D \frac{\partial}{\partial z_i} [\Phi_i(\mathbf{z})\rho(\mathbf{z})] = 0. \quad (10)$$

Further, due to the $v_{\mathbf{q}}$ -preserving nature of $K_{\mathbf{q}}(\mathbf{p}|\mathbf{p}')$ above, the right hand side of the Fokker-Planck equation (5) reduces to (see Appendix A.2 for more detailed calculations)

$$\begin{aligned} & \int \rho(\mathbf{z}')\lambda(\mathbf{q}', \mathbf{p}')\delta(\mathbf{q} - \mathbf{q}')K_{\mathbf{q}'}(\mathbf{p}|\mathbf{p}')d\mathbf{z}' - \rho(\mathbf{z})\lambda(\mathbf{z}), \\ & = \pi(\mathbf{q})C(\mathbf{q}) \int K_{\mathbf{q}}(\mathbf{p}|\mathbf{p}')v_{\mathbf{q}}(\mathbf{p}')d\mathbf{p}' - \rho(\mathbf{z})\lambda(\mathbf{z}) = 0, \end{aligned}$$

and hence Proposition 1 follows.

Notice that allowing the event rate to depend on the momentum \mathbf{p} requires that the momentum refresh distribution must be modified relative to simply preserving the BG distribution \mathbf{p} -marginal as in regular HMC and RHMC. Similar choices of Q are discussed by Fearnhead et al. (2018, Section 3.2.1) and Vanetti et al. (2018, Section 2.3.3). Further notice that the above results are easily modified to accommodate a general non-Gaussian \mathbf{p} -marginal (see e.g. Livingstone et al., 2019) of the (separable) BG distribution (see Appendix A.1,A.2) and a Riemann manifold variant (Girolami and Calderhead, 2011) (see Appendix A.3).

3.3 More on event specifications

Two special cases of the general event specification characterized by $\lambda = \lambda(\mathbf{q}, \mathbf{p})$ and (9) may be mentioned: for event rates not depending on \mathbf{p} , say $\lambda(\mathbf{z}) = \omega(\mathbf{q}) > 0$, implies that $v_{\mathbf{q}}(\mathbf{p}) = \mathcal{N}(\mathbf{p}|\mathbf{0}_d, \mathbf{M}) \forall \mathbf{q}$ and momentums may be updated as in generalized HMC (Horowitz, 1991), namely

$$K_{\mathbf{q}}(\mathbf{p}|\mathbf{p}') = \mathcal{N}(\mathbf{p}|\phi\mathbf{p}', \sqrt{1 - \phi^2}\mathbf{M}), \quad (11)$$

for some fixed Horowitz parameter $\phi \in (-1, 1)$. Secondly, assuming further structure on $\lambda = \lambda(\mathbf{q}, \mathbf{p})$ may lead to tractable sampling directly from $v_{\mathbf{q}}(\mathbf{p})$. Examples include:

- λ allows the representation $\lambda(\mathbf{z}) = b(\mathbf{q}, \mathbf{p}^T \mathbf{M}^{-1} \mathbf{p})$ for suitably chosen function $b : \mathbb{R}^d \times \mathbb{R}^+ \mapsto \mathbb{R}^+$. Then, $v_{\mathbf{q}}(\mathbf{p})$ is an elliptically contoured distribution (see e.g. Cambanis et al., 1981) which typically allows efficient independent sampling.
- $\log(\lambda(\mathbf{z}))$ is a quadratic function in \mathbf{p} for each \mathbf{q} . Then $v_{\mathbf{q}}(\mathbf{p})$ is Gaussian, which admit straight forward independent or autocorrelated momentum refreshes.

Event specification	λ	$K_{\mathbf{q}}(\mathbf{p} \mathbf{p}')$	Interpretation
1	$\frac{1}{\beta}$	$\mathcal{N}(\mathbf{p} \phi\mathbf{p}', \sqrt{1-\phi^2}\mathbf{M}), \phi \in (-1, 1)$	Time between events is $Exp(\beta)$, autocorrelated momentum refreshes
2	$\frac{1}{\beta}\sqrt{\mathbf{p}^T\mathbf{M}^{-1}\mathbf{p}}$	$\propto \sqrt{\mathbf{p}^T\mathbf{M}^{-1}\mathbf{p}} \exp(-\frac{1}{2}\mathbf{p}^T\mathbf{M}^{-1}\mathbf{p})$ $\sim \sqrt{\frac{r}{\mathbf{y}^T\mathbf{y}}}\sqrt{\mathbf{M}}\mathbf{y},$ where $\mathbf{y} \sim N(\mathbf{0}_d, \mathbf{I}_d), r \sim \chi^2(d+1)$	Arc-length of between-events (standardized) position trajectory is $Exp(\beta)$, independent momentum refreshes

Table 1: The event specifications applied in the remainder of this text. In all cases β is a tuning parameter, where larger β s on average correspond to less frequent events/longer inter-event trajectories. For specification 2, arc-lengths of position-trajectories are calculated in the Mahalanobis distance $d(\mathbf{q}, \mathbf{q}') = \sqrt{(\mathbf{q} - \mathbf{q}')^T \mathbf{M} (\mathbf{q} - \mathbf{q}')}$ as \mathbf{M}^{-1} is assumed to be some approximation/reflect the scales of the covariance matrix of $\pi(\mathbf{q})$.

These cases, and the rather rudimentary specific choices committed below, are by no means exhausting the possibilities, and further research taking (9) as vantage point is currently under way. Avenues actively explored include Metropolized versions of $K_{\mathbf{q}}(\mathbf{p}|\mathbf{p}')$ similar to (11) but for general \mathbf{p} -dependent event rates. Further work is done to obtain processes that have intervals between events well adapted to the target distribution similarly to e.g., the NUTS algorithm. Finally, it should also be mentioned that $K_{\mathbf{q}}(\mathbf{p}|\mathbf{p}')$ may in principle be selected first for some desirable purpose (e.g., momentum-refreshes that are over-dispersed relative to \mathbf{M} to allow for jumps between modes), with the event rate subsequently chosen to so that $K_{\mathbf{q}}$ is invariant with respect to $v_{\mathbf{q}}$.

Further notice that there is a fundamental difference between changing the BG- \mathbf{p} -marginal (see e.g. Livingstone et al., 2019) and selecting a \mathbf{p} -dependent event rate so that the moment-refreshes must preserve a $v_{\mathbf{q}}(\mathbf{p})$ different from $\mathcal{N}(\mathbf{p}|\mathbf{0}_d, \mathbf{M})$. The former case changes also the deterministic dynamics, whereas the latter does not. Hence, there is *an additional degree of freedom* in the present setup in that one may fix the Hamiltonian (and hence dynamics) first, and then modify the momentum refreshes afterwards by suitable choices of the event rate.

3.4 Specific event specifications

Table 1 provides the specific event specifications used in the remainder of this text. The former is RHMC with Horowitz type momentum refreshes (11), whereas specification 2 involves independent updates according to an elliptically contoured momentum refresh distribution $v_{\mathbf{q}}$.

Interestingly, the large λ limit of the \mathbf{q} -component of the PDMP, i.e. $\mathcal{Q}(t)$, for specification 1, is a Brownian motion-driven preconditioned Langevin process (see e.g. Roberts and Rosenthal, 1998) (see Appendix

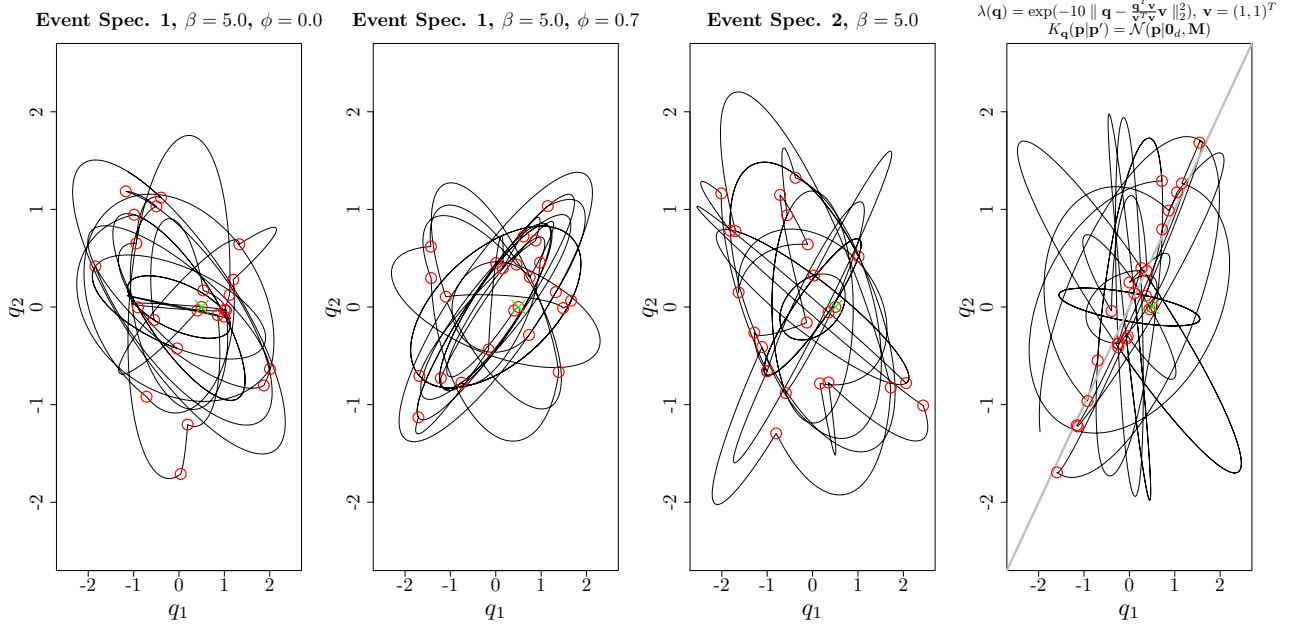


Figure 2: Examples of \mathbf{q} -coordinate of continuous time HMC trajectories with different event specifications for a bivariate standard Gaussian target distribution $\pi(\mathbf{q})$. In all cases, $\mathbf{M} = \mathbf{I}_2$ and the shown trajectories correspond 100 units of time t . Events are indicated with red circles, and the common initial \mathbf{q} -coordinate is indicated with a cross. In the rightmost panel, an event rate favoring events when the distance between the \mathbf{q} -coordinate and its projection onto the subspace spanned by $\mathbf{v} = (1, 1)^T$ (indicated by a gray line) is small.

A.4)

$$d\mathcal{Q}(t) = \frac{1}{2}\mathbf{M}^{-1}\nabla_{\mathbf{q}}\log\tilde{\pi}(\mathcal{Q}(t)) + \mathbf{M}^{-\frac{1}{2}}d\mathbf{W}(t). \quad (12)$$

Here $\mathbf{W}(t)$ is a standard Brownian motion and $\mathbf{M}^{-\frac{1}{2}}$ is any matrix square-root of \mathbf{M}^{-1} .

Specification 2 is a first attempt at providing event rates where the length of the between-event trajectories is chosen dynamically. Specifically, the event specification is chosen so that $\beta\int_0^v\lambda(\varphi_s(\mathbf{z}))ds = \beta\Lambda(v; \mathbf{z})$ is exactly the arc-length (in the Mahalanobis distance $d(\mathbf{q}, \mathbf{q}') = \sqrt{(\mathbf{q} - \mathbf{q}')^T\mathbf{M}(\mathbf{q} - \mathbf{q}')}$ for standardization, see Appendix Section A.5 for details) of the position coordinate when \mathbf{z} was the state of the process immediately after the last event. For this specification, $\mathbf{v}_{\mathbf{q}}$ allows straight forward sampling as it is an elliptically contoured distribution (see Table 1).

Note that $\beta = O(d^{1/2})$ is needed to ensure $E(\lambda) = O(1)$, but also result in that $\text{Var}(\lambda) = O(d^{-1})$ under the BG-distribution. Further, $\mathbf{v}_{\mathbf{q}}$ converges to $N(\mathbf{0}_d, \mathbf{M})$ for large d (as $\text{Var}(r/\mathbf{y}^T\mathbf{y})$ in Table 1 is $O(d^{-1})$). Hence, for large d one would expect a similar behavior of specifications 1 and 2.

3.5 Illustrative examples

Figure 2 shows examples of the trajectories of the \mathbf{q} -coordinate under continuous time HMC process for different event specifications for a bivariate standard Gaussian target. It is seen that the nature of the trajectories differs, with event specification 1, $\phi = 0.7$, visiting a somewhat narrower “range” of orbits relative to that of event specification 1, $\phi = 0$. For event specification 1, there is quite large variation in the “how much ground” each between-event trajectory is covering (several of the between-event trajectories go through multiple identical cycles), whereas the arc-lengths have less variation under specification 2. Recall still that arc-lengths are only in expectation equal under event specification 2 as u appearing in (4) are exponentially distributed.

The rightmost panel of Figure 2 is included as an illustration of the flexibility afforded by GRHMCs as defined in Section 3.1. An event-rate favoring events occurring when the \mathbf{q} -coordinate is close to (somewhere on) the subspace defined by $\mathbf{q}_1 = \mathbf{q}_2$ is considered. This is an example of a process where (unlike RHMC) the embedded discrete time process obtained by considering only the configuration at events is clearly off target, whereas the continuous time GRHMC process still has the desired stationary distribution. Such processes may be an avenue for obtaining between events dynamics amounting to (an integer multiple) of approximately half orbits. However, the selection of event-favoring subspaces for general non-Gaussian target distributions requires further research. From now on, only event specifications 1, $\phi = 0$ and 2 are considered.

3.5.1 Moment estimation and “super-convergence”

To gain some initial insight into the behavior of moment estimation based on NGRHMC processes, 10000 trajectories of were generated for 4 zero mean, unit variance univariate targets $\pi(\mathbf{q}_1)$. Each trajectory was of (time) length $T = 1000\frac{\pi}{2}$ preceded by an equal length of warmup. Event specification 1, $\phi = 0$, was used in all cases, and experiments were repeated for different values of the inter-event mean time β (see Table 1). Further, several different sampling strategies were applied to all produced trajectories. Root mean squared errors (RMSEs) of the $E(\mathbf{q}_1)$ -estimates are presented in Figure 3.

For the standard Gaussian distribution, exactly iid samples obtains when choosing trajectories of (time) length $\pi/2$ in the hypothetical HMC method (with exact dynamics, see Section 2.2). Thus, the (time) lengths of generated Hamiltonian flow (and thus essentially the computational cost) of NGRHMC and for 1000 iid-samples-producing hypothetical HMC transitions are the same. As a reference to the NGRHMC results, the RMSEs based on 1000 iid samples are indicated as horizontal lines in the plots. For the non-Gaussian targets, the cost of obtaining RMSEs corresponding to 1000 iid samples using HMC are likely somewhat higher, and thus the benchmarks are likely somewhat favoring HMC in a computational cost perspective in

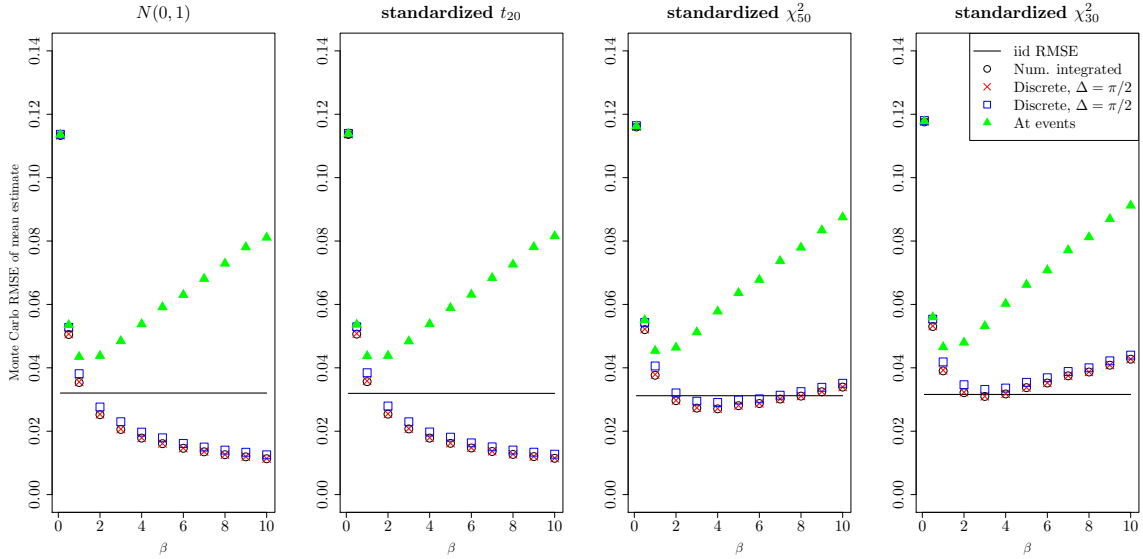


Figure 3: RMSE of estimates of $E(\mathbf{q}_1)$ from NGRHMC processes using event specification 1 for different values of the mean inter-event time parameter β . The panels correspond to the different univariate target distributions $\pi(\mathbf{q}_1)$, which all have zero mean and unit variance. Unit mass matrix $M = 1$ was used. The estimates of the mean are based on trajectories of length $T = 1000\frac{\pi}{2}$, and the RMSE estimates are based on 10000 independent replica for each value of β . Black circles correspond continuous sampling (7), red \times -s to 1000 equally spaced samples, blue squares to 500 equally spaced samples and green triangles to samples recorded at events only. The horizontal lines give the RMSE of 1000 iid samples. The results are obtained using the numerical methods described in Section 4.1 with $tol_a = tol_r = 0.001$.

these cases.

In all cases, low values of β (frequent events) result in poor results, as the continuous time process approaches the Langevin limit (12). The most striking feature of the plot is that for continuous (black circles) or high frequency sampling (red \times) of the trajectories, RMSEs for the symmetric targets ($N(0,1)$, standardized t_{20}) decreases monotonically in β , and for the highest $\beta = 10.0$ considered is only around 35 percent of the benchmark in the $N(0,1)$ case. In the univariate Gaussian target case, this behavior obtains as the between-event Hamiltonian dynamics, $\mathbf{q}_1(t)$, averaged over time, i.e. $\frac{1}{t} \int_0^t \mathbf{q}_1(s) ds$, converges to the mean of the target as $t \rightarrow \infty$, *regardless of the initial configuration* $\mathbf{z}(0)$ (see below and Appendix B). Thus, in the Gaussian case, momentum refreshes are not necessary for unbiased estimation of $E(\mathbf{q}_1)$. It appears this is also the case for the standardized t_{20} -distribution, but this has not been proved formally so far.

For the non-symmetric targets, standardized χ_{50}^2 and standardized χ_{30}^2 , such monotonous behavior is not seen as momentum refreshes are certainly necessary to obtain high quality estimates. Too infrequent refreshes (i.e., high β) result in higher variance from exploring too few energy level sets. For intermediate values of β , the continuous- or high frequency sampling estimates are still better than or on par with the iid benchmark, where the edge is lost towards more skewness in the target distribution.

As mentioned in Section 2.3, the continuous time trajectories can either be sampled at discrete times (6) or continuously (in practice integrated numerically within the ODE solver, see below for details) over time (7), where the former may be thought of as a crude quadrature approximation to the latter. From Figure 3, it is evident that there is little difference in the high frequency ($\Delta = \pi/2$) discrete time sampling and continuous sampling. The efficiency deteriorates somewhat with more infrequent ($\Delta = \pi$) discrete sampling (blue \square). As will be clear in the next section, continuous estimates (7) require minimal additional numerical effort, and it seems advisable always to use these for moment calculations, whereas rather frequent discrete samples should be used for other tasks.

The green triangles represent results obtained when sampling the process only at event times using the same amount of Hamiltonian trajectory. It is seen that this practice, which does not exploit the “between-events” trajectories, generally lead to inferior results. The exception is in the random walk-like domain, where frequent events (and thus sampling) occur, but in this case the underlying process only slowly explores the target distribution.

3.6 Choosing event intensities

The time average property under the univariate Gaussian, illustrated in the left panel of Figure 3 generalizes to multivariate Gaussian targets $\pi(\mathbf{q}) = \mathcal{N}(\mathbf{q}|\mu, \Sigma)$ as well. Namely, it can be shown (see Appendix B) that the between-events dynamics $\mathbf{q}(\tau)$ admit unbiased estimation of μ without momentum refreshes, i.e.

$$\frac{1}{T} \int_0^T \mathbf{C}\mathbf{q}(\tau)d\tau \xrightarrow{T \rightarrow \infty} \mathbf{C}\mu, \quad \mathbf{C} \in \mathbb{R}^{p \times d}, \quad (13)$$

regardless of the initial configuration $\mathbf{z}(0)$.

Of course, the Gaussian case is not particularly interesting per se. However, one would presume that for near Gaussian target distributions (which is frequently the case in Bayesian analysis applications due to Bernstein-Von Mises effects), the left-hand side (13) would have only a small variation in $\mathbf{z}(0)$ for large T . Hence such situations would benefit from quite low event intensities/long durations between events and would allow for very small Monte Carlo variations in moment estimates akin to those shown in the two leftmost panels of Figure 3 even in high-dimensional applications.

Still, the fast convergence results above are restricted to certain moments of certain target distributions. It is instructive (and sobering) to look at the estimation of the second order moment of a univariate standard Gaussian target distribution (with $\mathbf{M} = 1$). In this case,

$$\frac{1}{T} \int_0^T \mathbf{q}_1^2(\tau)d\tau \xrightarrow{T \rightarrow \infty} \frac{1}{2} (\mathbf{q}_1^2(0) + \mathbf{p}_1^2(0)),$$

i.e. the dependence on the initial configuration $\mathbf{z}(0)$ does not vanish as the time between events grows, and the second order moment cannot be estimated reliably without momentum refreshes.

For a fixed budget of Hamiltonian trajectories, a non-Gaussian target and/or a non-linear moment, say $E(g(\mathbf{q}))$, and the event rate tradeoff will have at the endpoints:

- For “large β ”, variation in the GRHMC moment estimate is mainly due to variation between energy level sets, i.e. the variance of $\lim_{T \rightarrow \infty} \int_0^T g(\mathbf{q}(t)) dt$ as a function of the initial configuration $\mathbf{z}(0)$.
- For “small β ”, variation in the GRHMC moment estimate comes mainly from that the underlying process \mathcal{Z}_t reverts to a random walk-like behavior (Langevin-dynamics for constant event rate).

The location of the optimum between these extremes (see e.g., the two right-most panels in Figure 3) inherently depends both on the target distribution and the collection of moments, say $E(g_1(\mathbf{q})), \dots, E(g_m(\mathbf{q}))$, one is interested in. More automatic choices of event rate specifications will be explored in the numerical experiments discussed below.

4 Numerical implementation

The proposed methodology relies on quite accurate simulation of the Hamiltonian trajectories and associated functionals of the type (7). This section summarizes numerical implementation of these quantities based on Runge-Kutta-Nystöm (RKN) methods (see e.g. Hairer et al., 1993, Chapter II.14). The reader is referred to Hairer et al. 1993 for more background on general purpose ODE solvers.

In what follows, τ is used as the time index of the between-events Hamiltonian dynamics (as opposed to PDMP process time t), and it is convention that τ is reset to zero immediately after each event. RKN methods are particularly well suited for time-homogenous second order ODE systems on the form

$$\dot{\mathbf{y}}(\tau) = \mathbf{F}(\mathbf{y}(\tau)), \mathbf{y} \in \mathbb{R}^n, \mathbf{F} : \mathbb{R}^n \mapsto \mathbb{R}^n, \quad (14)$$

subject to the initial conditions $\mathbf{y}(0) = \mathbf{y}_0, \dot{\mathbf{y}}(0) = \mathbf{z}_0$. Notice that when \mathbf{F} does not depend on $\dot{\mathbf{y}}(\tau)$, RKN methods are substantially more efficient than applying conventional Runge Kutta methods to an equivalent coupled system of $2n$ first order equations, say $\dot{\mathbf{y}}(\tau) = \mathbf{w}(\tau), \dot{\mathbf{w}}(\tau) = \mathbf{F}(\mathbf{y}(\tau))$.

A wide range of numerical methods have been developed specifically for the dynamics of Hamiltonian systems (see e.g. Sanz-Serna and Calvo, 1994; Leimkuhler and Reich, 2004). Such methods typically conserve the symplectic- and time-reversible properties of the true dynamics, and hence provide reliable long-term simulations over many (quasi-)orbits. However, for shorter time spans, typically on the order of up to a few

(quasi-)orbits, such symplectic methods have no edge over conventional methods for second order ODEs (see e.g. Sanz-Serna and Calvo, 1994, Section 9.3).

4.1 Numerical solution of dynamics and functionals

In the numerical implementation used in the present work, the between-events Hamiltonian dynamics are reformulated in terms of the second order ODE

$$\ddot{\mathbf{q}}(\tau) = \mathbf{M}^{-1}\nabla_{\mathbf{q}}\log(\mathbf{q}(\tau)), \quad (15)$$

which is to be solved for $(\mathbf{q}(\tau), \dot{\mathbf{q}}(\tau))$. The dynamics of (15) are equivalent to the dynamics of (2) when the initial conditions $(\mathbf{q}(0), \dot{\mathbf{q}}(0) = \mathbf{M}^{-1}\mathbf{p}(0))$ are applied, and the momentum variable for any τ is recovered via $\mathbf{p}(\tau) = \mathbf{M}\dot{\mathbf{q}}(\tau)$.

Further, recall that the proposed methodology relies critically on the ability to calculate between-events Hamiltonian dynamics functionals on the form

$$\mathbf{r}_k(\tau) = \int_0^\tau \mathcal{M}_k(\mathbf{q}(s))ds, \quad k = 1, \dots, p, \quad (16)$$

for a suitably chosen monitoring function $\mathcal{M} : \mathbb{R}^d \rightarrow \mathbb{R}^p$, e.g., for *integrated event intensities* Λ (4) and continuous sampling (7). To this end, first observe that $\mathbf{r}(\tau) = \dot{\mathbf{R}}(\tau)$ whenever $\ddot{\mathbf{R}}(\tau) = \mathcal{M}(\mathbf{q}(\tau))$, with initial conditions $\mathbf{R}(0) = \mathbf{0}_p$, $\dot{\mathbf{R}}(0) = \mathbf{0}_p$. Hence by augmenting (15) with the monitoring function, i.e.

$$\begin{bmatrix} \ddot{\mathbf{q}}(\tau) \\ \ddot{\mathbf{R}}(\tau) \end{bmatrix} = \begin{bmatrix} \mathbf{M}^{-1}\nabla_{\mathbf{q}}\log(\mathbf{q}(\tau)) \\ \mathcal{M}(\mathbf{q}(\tau)) \end{bmatrix}, \quad (17)$$

a system on the form (14) is obtained. When solved numerically, (17) produces solutions both for the dynamics (2 or 15) and the dynamics functional (16). Implemented in this manner, the adaptive step size methodology (discussed in Appendix C) controls both the numerical error in the Hamiltonian dynamics and the functionals concurrently (in contrast to Nishimura and Dunson (2020) where integrator step sizes are kept fixed and intermediate integrator steps are included in averages based on an accept/reject mechanism).

In this work, the 6th order explicit embedded pair RKN method RKN6(4)6FD of Dormand and Prince (1987, Table 2) was used to solve (17). Each step of RKN6(4)6FD requires 5 evaluations of the right-hand side of (17), but of course being a higher order method, the step sizes may typically be substantially larger than the stability limit of e.g., the leap frog method. Since the solution to $\mathbf{R}(\tau)$ is not required per se, trivial modifications of the mentioned RKN method were done so that it solves only for $\mathbf{s}(\tau) = (\mathbf{q}(\tau), \dot{\mathbf{q}}(\tau), \mathbf{r}(\tau))$.

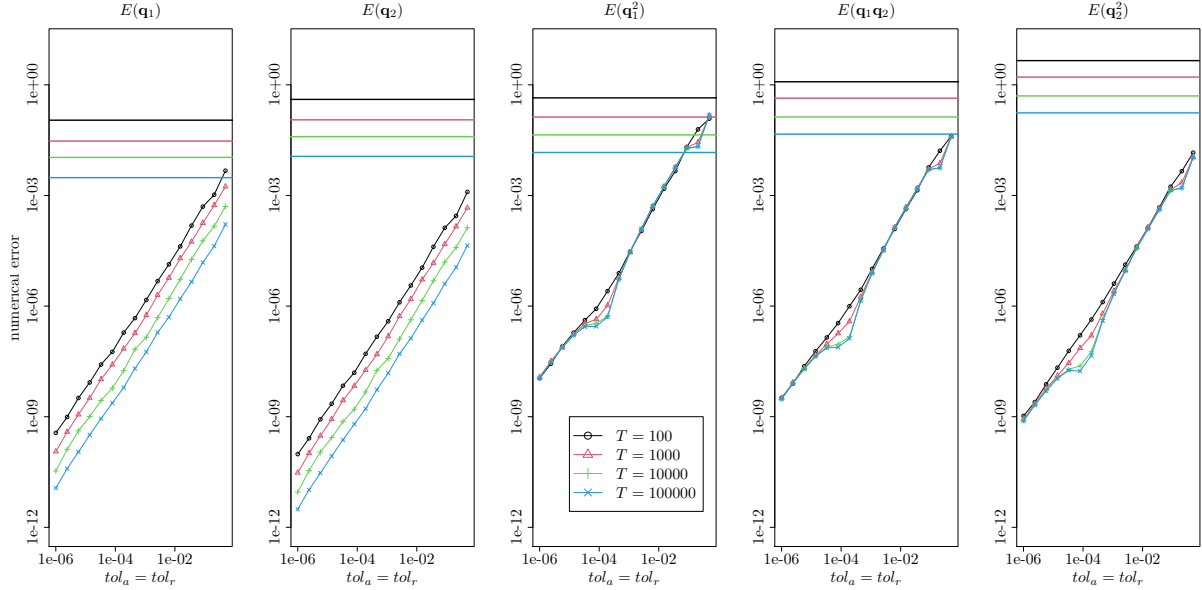


Figure 4: Numerical errors incurred by RKN integration on the estimation the first and second order moments of a bivariate Gaussian target distribution. The numerical errors are relative to a NGRHMC trajectory using the same random numbers but with exact Hamiltonian dynamics. Both exact and numerically integrated results are based on continuous sampling. The horizontal axis gives the error tolerances (in all cases with $tol_a = tol_r$) applied in the numerical integrator, and both horizontal and vertical axis are logarithmic. Dotted lines indicate the root mean squared errors associated with estimating the indicated moments across many exact NGRHMC trajectories of different length T .

Further details, and a full algorithm may be found in Section C in the Appendix. It is also worth noticing that simpler, but less efficient variants of the above algorithm may be written in high level languages with access to off-the-shelf ODE solvers. Section G in the Appendix gives an example written in R.

4.2 Do numerical errors influence results?

To assess how the application of (un-corrected) RKN numerical integrators for the Hamiltonian dynamics influences overall Monte Carlo estimation, a small simulation experiment was performed. Specifically, a $N(\mathbf{0}_2, \Sigma)$ target distribution with

$$\Sigma = \begin{bmatrix} 1 & 2 \\ 2 & 8 \end{bmatrix}, \mathbf{M} = \mathbf{I}_2, \lambda = \frac{1}{10} \text{ and } Q(\mathbf{p}|\mathbf{z}') = \mathcal{N}(\mathbf{p}|\mathbf{0}_2, \mathbf{M}), \quad (18)$$

was used. Due to the Gaussian nature of the target distribution, the Hamiltonian dynamics are available in closed form, and hence allow the comparison with the numerically integrated counterparts. RHMC trajectories based both on exact and numerically integrated dynamics were used to estimate the mean and raw second order moments of the target using continuous sampling. The same initial configuration $\mathcal{Z}(0)$ and

the same random numbers were used so that errors in the estimators based on numerical integration are due only to RKN integration. Figure 4 shows the RMSEs between estimates from numerically integrated- and exact RHMC trajectory for different values of T and the absolute (relative) RKN integrator error tolerance tol_a (tol_r) (see Appendix C for details). All results are based on independent 50 replications. Also indicated in the plots as horizontal lines are the RMSEs associated with estimating the said moments (across multiple independent trajectories) based on RHMC with exact dynamics.

From Figure 4, it is seen that except for very large values of $tol_a = tol_r$, the numerical errors are very small relative to the exact estimator RMSEs. From the plots, absolute and relative error tolerances of around 0.001 appear to be more than sufficient for this case. Interestingly, it is seen that there is no apparent buildup of numerical errors in the longer trajectories, suggesting that the incurred errors are not systematically accumulating and biasing the estimation in any direction. Of course, this limited experiment does not rule out such biasing behavior in general. However, the overall the finding here indicate that quite lax error tolerances are sufficient to make the numerical errors be negligible relative to overall Monte Carlo variation.

4.3 Automatic selection of tuning parameters

A key aim of developing NGRHMC processes is to enable the implementation of an easy to use and general-purpose code. For this purpose, automatic selection of tuning parameters is important. This Section describes the routines for tuning the mass matrix \mathbf{M} and scaling the event intensity used in the computations described shortly.

4.3.1 Tuning of mass matrix

In the present work, only a diagonal mass matrix $\mathbf{M} = \text{diag}(m_1, \dots, m_d)$ is considered. Two approaches for choosing each of m_1, \dots, m_d are considered, both exploiting the ability to numerically calculate temporal averages by augmenting the monitoring function \mathcal{M} .

In the former approach which will be referred to as VARI (variance, integrated), m_i^{-1} is simply set equal to the temporal average estimate of $\text{Var}(\mathbf{q}_i)$, i.e.

$$\int_0^{t^*} \mathcal{Q}_i^2(s) ds - \left[\int_0^{t^*} \mathcal{Q}_i(s) ds \right]^2,$$

at every event time t^* during the warmup period.

In cases where the marginal variances are less informative with respect to the local scaling of the target distribution, e.g., in the presence of strong non-linearities or multimodality, a second approach referred to as

ISG (integrated squared gradients) may also be pursued. Here the overarching idea for choosing each of m_1, \dots, m_d is to make the square of each element of the right-hand side of (15), averaged over *each integrator step*, in expectation over all integrator steps, to be equal to 1. This approach is mainly motivated out of numerical efficiency considerations, where regions of the target distribution requiring many steps (with short step sizes due to strong forces $\nabla_{\mathbf{q}} \log \tilde{\pi}(\mathbf{q})$) are disproportionately weighted when choosing the mass matrix.

More explicitly, let the j th integrator step (during the warmup period) be originating at time τ_j and have time step size ε_j . Then the mass matrix diagonal m_i is taken to be an exponential moving average (over j) of

$$\frac{1}{\varepsilon_j} \int_{\tau_j}^{\tau_j + \varepsilon_j} [\nabla_{\mathbf{q}} \log \tilde{\pi}(\mathbf{q}(s))]_i^2 ds.$$

Notice that the integrated squared gradients are available at negligible additional cost by augmenting \mathcal{M} in the ODE system (17) with moment functions $[\nabla_{\mathbf{q}} \log \tilde{\pi}(\mathbf{q})]_i^2$, $i = 1, \dots, d$. Further notice that for a $N(\mu, \mathbf{P}^{-1})$ target distribution, where $E_{\pi}([\nabla_{\mathbf{q}} \log \tilde{\pi}(\mathbf{q})][\nabla_{\mathbf{q}} \log \tilde{\pi}(\mathbf{q})]^T) = \mathbf{P}$, this approach may (modulus variability in integrator step size) be seen as a way to *directly estimate the precision matrix diagonal elements*.

4.3.2 Tuning of event rates

The methodology for tuning the event rates relies on the following representation of a general event rate λ :

$$\lambda(\mathbf{q}, \mathbf{p}) = \frac{1}{\gamma\beta} \bar{\lambda}(\mathbf{q}, \mathbf{p}), \quad \gamma > 0, \beta > 0,$$

where $\bar{\lambda}$ is a “base line” event rate (e.g., $\bar{\lambda} = 1$ for event specification 1 and 2, and $\bar{\lambda} = \sqrt{\mathbf{p}^T \mathbf{M}^{-1} \mathbf{p}}$ for event specification 2). Here γ is a user-given scale factor, say in the range 1 to 20, chosen in the higher range if one expects good performance with infrequent moment refreshes (see Section 3.6). Finally, β is tuned automatically to reflect each particular target distribution and event specification.

Suppose $\iota(\mathbf{z})$ is the distribution the state immediately after events (which is equal to $\rho(\mathbf{z})$ for RHMC but may also differ substantially relative to $\rho(\mathbf{z})$ as seen in the rightmost panel of Figure 2). The objective of the automatic event rate tuning is given by

$$E_{\mathbf{z}(0) \sim \iota(\mathbf{z})} \beta^{-1} \Upsilon(\mathbf{z}(0)) = 1, \quad \text{where } \Upsilon(\mathbf{z}(0)) = \int_0^{\omega(\mathbf{z}(0))} \bar{\lambda}(\mathbf{q}(\tau), \mathbf{p}(\tau)) d\tau, \quad (19)$$

and where ω is the “U-turn” time (Hoffman and Gelman, 2014)

$$\omega(\mathbf{z}(0)) = \inf \{ \tau > 0 : (\mathbf{q}(\tau) - \mathbf{q}(0))^T \mathbf{p}(\tau) < 0 \},$$

of the dynamics (2) initialized at $\mathbf{z}(0)$ (See also Wu et al., 2018, for a similar development). The rationale behind (19) is that (for $\gamma = 1$) the expected integrated event rate Λ (see Equation 4) evaluated at corresponding U-turn time is equal to $E(u)$.

In the present implementation, $\Upsilon(\mathbf{z}(0))$ is computed for each event during warmup with $\mathbf{z}(0)$ being the state immediately after the events. Subsequently, β^{-1} is updated (also during the warmup period only) at each event according to an exponential moving average over the already computed Υ s. The exponential moving average is used as the older realizations of Υ are typically recorded with a different mass matrix encountered earlier in the mass matrix adaptation process. Computing $\Upsilon(\mathbf{z}(0))$ for each event incurs only modest additional costs, since Υ is a scalar integrated quantity computed over Hamiltonian dynamics that are integrated numerically anyway. However, if the next event occurs before the U-turn time ω , further integration steps are performed until ω is reached. The additional (post-event) Hamiltonian dynamics used to locate ω are subsequently discarded.

5 Numerical experiments

This section considers numerical experiments and benchmarking of the proposed method against the NUTS-HMC implementation in Stan (rstan version 2.21.2). Like Stan, the proposed methodology has been implemented as an R package (pdphmc) with main computational tasks done in C++, and relies, like rstan, on the Stan Math Library (Carpenter et al., 2017) for automatic differentiation and probability- and linear algebra computations.

All computations in this section were carried out on a 2020 Macbook pro with a 2.6 GHz Intel Core i7 processor, under R version 4.0.3. In line with the findings in Section 4.2, the default integrator tolerances $tol_a = tol_r = 0.001$ are used for pdphmc unless otherwise noted. The package pdphmc, and code and data for reproducing the reported results is available at <https://github.com/torekleppe/PDPHMCpaperCode>.

In order to compare the performance of the methods, their Effective Sample Size (ESS) (Geyer, 1992) per computing time (see e.g. Girolami and Calderhead, 2011) is taken as the main statistic. Consider a sample dependent of dependent random variables η_i , $i = 1, \dots, N$, each having the same marginal distribution. The ESS gives the number of hypothetical iid samples (with distribution equal to that of η_1) required to obtain a mean estimator with the same variance as $N^{-1} \sum_{i=1}^N \eta_i$. An ESS-based approach is taken also here, but in order to obtain ESSes for moments estimated by for integrated quantities (7), the following approach was

taken: For a given number of samples, say N , rewrite the left-hand side of (7) as

$$\frac{1}{T} \int_0^T g(\mathcal{Z}(t))dt = \frac{1}{N} \sum_{i=1}^N \eta_i, \text{ where } \eta_i = \Delta^{-1} \int_{(i-1)\Delta}^{i\Delta} g(\mathcal{Z}(t))dt, \Delta = \frac{T}{N}. \quad (20)$$

Let $\widehat{ESS}_i(\eta_i)$ denote an estimator of the ESS of dependent sample η_i . Then

$$\frac{\widehat{Var}_i(g(\mathcal{Z}(\Delta i)))}{\widehat{Var}_i(\eta_i)} \widehat{ESS}_i(\eta_i) \quad (21)$$

is taken to be an estimator of ESS represented by moment estimator $T^{-1} \int_0^T g(\mathcal{Z}(t))dt$, expressed in terms of iid samples of $g(\mathbf{q})$. Equation 21 takes into account both that $\widehat{Var}_i(\eta_i)$ tends to be smaller than $\widehat{Var}_i(g(\mathcal{Z}(\Delta i)))$ due to the temporal averaging in (20), but on the other hand η_i tends to exhibit a stronger autocorrelation than discrete time samples $g(\mathcal{Z}(\Delta i))$. Throughout this text, the ESS estimation procedure in `rstan` (see R-function `rstan::monitor()`, output “`n_eff`”) was used for estimating ESS from samples. In addition, the largest (over sampled quantities) Gelman-Rubin \hat{R} statistics ($\max \hat{R}$) (Gelman et al., 2014) were computed using the same function. For `pdphmc`, the reported $\max \hat{R}$ are computed for the discretely sampled processes.

Comparing the performance of different MCMC methods is intrinsically hard. Care has been taken so that all code is written in the same language and compiled with the same compiler on the same computer and so on. Still, in the present context one must also consider that `rstan` is based on an “exact” MCMC scheme whereas `pdphmc` will in general be subject to (arbitrarily small, at the cost of more computing,) biases stemming from the use of uncorrected numerical integration. On the other hand, as demonstrated e.g., in Figure 1, chains of finite length generated by `rstan` may fail to reflect the target distribution in cases where no visible bias is exhibited by `pdphmc` due to the adaptive nature of the applied integrators. The relative weighting of these features naturally depends on the application at hand, and therefore preclude strong conclusions regarding the relative performance of the methods.

In what follows, three numerical experiments are presented. A further experiment, based on a crossed random effects model for the Salamander data is described in Section D of the Appendix. For the Salamander data, `pdphmc` is found to be on par or somewhat more efficient than `rstan`.

5.1 Funnel distribution

The Funnel distribution $\mathbf{q}_1 \sim N(0, 1)$, $\mathbf{q}_2 | \mathbf{q}_1 \sim N(0, \exp(3\mathbf{q}_1))$ (funnel distributions may be traced back to Neal, 2003), constituting the first numerical example, has already been encountered in Section 2.2 and Figure 1. This very simple example may be considered as a “model problem” displaying similar behavior

as for targets associated with Bayesian hierarchical models (where q_1 plays the role of latent field log-scale parameter, and q_2 plays the role of the latent field it self).

For both rstan and pdphmc, 10 independent chains/trajectories were run with identity mass matrices. For rstan, each of these chains had 10,000 transitions with 5,000 discarded as warmup. The number of warmup iterations is larger than the default 1000 to allow for best possible integrator step size adaptation. The remaining tuning parameters of rstan are the default. Note that rstan outputs a substantial number of warnings related to diverged transitions for all values of δ .

For pdphmc, the trajectories were of length $T = 100,000$, sampled discretely $N = 10,000$ times and with the former half of samples discarded as warmup. For such high sampling frequency, continuous samples yield similar results as the discrete samples, and are not discussed further here. A constant event rate $\lambda = \beta^{-1}$ was applied, and β was adapted with scale factor $\gamma = 2$ using the methodology described in Section 4.3.2. The adaptive selection resulted in values of β between 2.1 and 4.7 across the 10 trajectories, which again translates to between 0.21 and 0.48 discrete time samples per (between-events) Hamiltonian trajectory.

It has already been confirmed visually from Figure 1 that the output of rstan does not fully explore the target distribution as fixed time step size integration is broadly speaking unsuitable for this problem. Consequently, ESSes for rstan are not presented. pdphmc produces around 800 effective samples per second for the log-scale parameter \mathbf{q}_1 . This is close to double what one obtains by calculating time-weighted ESS for the (still defective) $\delta = 0.999$ rstan chains, indicating the the proposed methodology is highly competitive for difficult problems (as even smaller fixed time steps would be required to obtain proper convergence). Further, the default integrator tolerances $tol_a = tol_r = 0.001$ lead to biases (relative to the theoretical process) that are not detectable from the right panel of Figure 1.

5.2 Smile-shaped distribution

To further explore the performance of pdphmc applied to a highly non-linear target distributions; the “smile”-shaped distribution

$$\mathbf{q}_k | \mathbf{q}_1 \sim N(\mathbf{q}_1^2, 0.5^2), \quad k = 2, \dots, 11, \quad (22)$$

$$\mathbf{q}_1 \sim N(0, 1). \quad (23)$$

is considered. The results for various settings of pdphmc and rstan are given in Table 2. From the Table, it is seen that rstan has substantial convergence problems with the largest Gelman-Rubin $\hat{R} > 1.05$, whereas the various settings of pdphmc reliably explores the target. Choosing longer trajectories ($\gamma = 10$) results in higher sampling efficiency for the marginally standard Gaussian \mathbf{q}_1 , whereas for the non-Gaussian components $\mathbf{q}_{2:11}$,

γ	sampling	\mathbf{q}_1		$\min_{k \in \{2,11\}} ESS(\mathbf{q}_k)$		$\max_{k \in \{2,11\}} ESS(\mathbf{q}_k)$		$E(\mathbf{q}_1)$	$E(\mathbf{q}_2)$	CPU time
		ESS	$\frac{ESS}{CPU\ time}$	ESS	$\frac{ESS}{CPU\ time}$	ESS	$\frac{ESS}{CPU\ time}$	(exact = 0)	(exact = 1)	(s)
rstan ($\max \hat{R} = 1.247$)										
pdphmc, event specification 1, $\phi = 0$ ($\gamma = 2 : \max \hat{R} = 1.006, \gamma = 10 : \max \hat{R} = 1.015$)										
2	D	1323	779	1065	627	1215	716	-0.02	1.03	1.7
2	C	1319	777	1115	657	1150	678	-0.02	1.02	
10	D	2213	1304	608	358	634	374	0.01	1.00	1.7
10	C	2233	1316	613	361	630	371	0.01	1.01	
pdphmc, event specification 2 ($\gamma = 2 : \max \hat{R} = 1.007, \gamma = 10 : \max \hat{R} = 1.009$)										
2	D	1094	645	1130	666	1183	697	-0.02	0.98	1.7
2	C	1094	645	1153	679	1184	698	-0.02	0.97	
10	D	2276	1341	920	542	967	570	0.01	1.03	1.7
10	C	2303	1357	927	546	948	559	0.01	1.03	

Table 2: Results for the “smile”-shaped target distribution (22,23). The results are based on 10 independent replica, and ESSes and ESSes per computing time (best in bold font) are from the combined results over these replica. For rstan, each replica consists of the 10,000 transitions, with the former 5,000 discarded as warmup. For pdphmc, ISG-type mass matrix, trajectories of length $T = 25,000$ divided evenly between warmup and sampling, and 1000 discrete samples were used. The presented CPU times are the total time spent by all chains/trajectories during the post warmup period. For each configuration of pdphmc, results from both discrete sampling (D) and continuous sampling (C) are presented.

shorter trajectories are more efficient. Comparing the event specifications 1 and 2, it is seen that none of them produces uniformly better results.

5.3 Logistic regression

The next example model is a basic logistic regression model

$$\mathbf{y}_i | \boldsymbol{\beta} \sim \text{Beroulli}(\mathbf{p}_i), \text{logit}(\mathbf{p}_i) = \mathbf{x}_{i,\cdot}^T \boldsymbol{\beta}, i = 1, \dots, n, \quad (24)$$

$$\boldsymbol{\beta} \sim N(\mathbf{0}_p, 100\mathbf{I}_p) \quad (25)$$

applied to the German credit data (see e.g. Michie et al., 1994) which has $n = 1000$ examples and $p = 25$ covariates (including a constant term). This example is included to measure the performance relative to rstan on an “easy” target distribution (Chopin and Ridgway, 2017).

Results for pdphmc and rstan are provided in Table 3. It is seen that rstan produces less variation in the ESSes across the different parameters than pdphmc, which presumably is related to the mass matrix adaptation. The discrete samples cases of pdphmc have a somewhat slower minimum ESS performance but on par or better median- and maximum ESS performance. For this target distribution, continuous samples for the first moment of $\boldsymbol{\beta} | \mathbf{y}$ substantially improves the performance of pdphmc relative to the corresponding discretely sampled counterparts in all cases.

γ	Sampling	$\min_j \widehat{ESS}(\beta_j)$		$\text{median}_j \widehat{ESS}(\beta_j)$		$\max_j \widehat{ESS}(\beta_j)$		CPU time
		ESS	$\frac{\text{ESS}}{\text{CPU time}}$	ESS	$\frac{\text{ESS}}{\text{CPU time}}$	ESS	$\frac{\text{ESS}}{\text{CPU time}}$	
rstan ($\max \hat{R} = 1.003$)								
		9676	2125	13450	2953	15812	3472	4.55
pdphmc, event specification 1 ($\gamma = 5 : \max \hat{R} = 1.011, \gamma = 20 : \max \hat{R} = 1.020$)								
5	D	11350	1425	23114	2903	40000	5023	7.96
5	C	18220	2288	32967	4140	71079	8926	
20	D	11853	1490	29752	3740	40000	5028	7.96
20	C	20423	2567	36019	4528	69623	8752	
pdphmc, event specification 2 ($\gamma = 5 : \max \hat{R} = 1.007, \gamma = 20 : \max \hat{R} = 1.027$)								
5	D	11281	1362	23185	2799	40000	4829	8.28
5	C	18317	2211	30771	3715	66928	8080	
20	D	12780	1565	32653	3999	40000	4899	8.16
20	C	20902	2560	43303	5304	70584	8645	

Table 3: ESSes and time weighted ESSes for the logistic regression model (24,25) applied to the German credit data. All figures are based on 10 independent chains/trajectories. For rstan, the default 1000 warmup transitions followed by 1000 sampling transitions were used. For pdphmc, a VARI mass matrix, $T = 5000$ divided evenly between warmup and sampling and 1000 discrete samples per trajectory were used.

6 Dynamic Inverted Wishart model for realized covariances

6.1 Model and data

As a large scale illustrative application of NGRHMC, the dynamic inverted Wishart model for realized covariance matrices (Golosnoy et al., 2012) of Grothe et al. (2019) is considered. Under this model, a time series of SPD covariance matrices $\mathbf{Y}_k \in \mathbb{R}^{G \times G}$, $k = 1, \dots, n$ are modeled independently inverted Wishart distributed conditionally on a latent time-varying SPD scale matrix Σ_k and a degree of freedom parameter $\nu > G + 1$, i.e.

$$\mathbf{Y}_k | \Sigma_k, \nu \sim \text{inv-Wishart}(\nu, \Sigma_k) \quad (26)$$

so that $E(\mathbf{Y}_k | \Sigma_k, \nu) = (\nu - G - 1)^{-1} \Sigma_k$. The time-varying scale matrix is in turn specified in terms of

$$\Sigma_k = \mathbf{H}[\text{diag}(\exp(\mathbf{x}_{1,k}), \dots, \exp(\mathbf{x}_{G,k}))]\mathbf{H}^T \quad (27)$$

where $\mathbf{H} \in \mathbb{R}^{G \times G}$ is a lower triangular matrix with $\mathbf{H}_{g,g} = 1$, $g = 1, \dots, G$. The remaining (strictly lower triangular) elements $\mathbf{H}_{i,j}$, $j = 1, \dots, G - 1, i = j + 1, \dots, G$, are unrestricted parameters. Finally, the log-scale factors $\mathbf{x}_{g,k}$ are a-priori independent (over g) stationary Gaussian AR(1) processes

$$\mathbf{x}_{g,k} = \boldsymbol{\mu}_g + \boldsymbol{\delta}_g(\mathbf{x}_{g,k-1} - \boldsymbol{\mu}_g) + \boldsymbol{\sigma}_g \varepsilon_{g,k}, \quad \varepsilon_{g,k} \sim \text{iid } N(0, 1), \quad k = 2, \dots, n, \quad g = 1, \dots, G, \quad (28)$$

$$\mathbf{x}_{g,1} \sim N(\boldsymbol{\mu}_g, \boldsymbol{\sigma}_g^2 / (1 - \boldsymbol{\delta}_g^2)), \quad g = 1, \dots, G, \quad (29)$$

		rstan	pdphmc, event spec. 1, $\gamma = 10.0$		pdphmc, event spec. 2, $\gamma = 10.0$	
	CPU time (S,A)	(14605, 72127)	(10629, 25244)		(10189, 24960)	
	$\max \hat{R}$	1.003	1.032		1.034	
	sampling		D	C	D	C
μ	ESS (min, max)	(14304, 18487)	(12906, 28173)	(14467, 28370)	(14749, 38387)	(14224, 41821)
	ESS/S (min, max)	(0.98, 1.27)	(1.21, 2.65)	(1.36, 2.67)	(1.45, 3.77)	(1.40, 4.10)
	ESS/A (min, max)	(0.20, 0.26)	(0.51, 1.12)	(0.57, 1.12)	(0.59, 1.54)	(0.57, 1.68)
σ	ESS (min, max)	(14757, 20011)	(28447, 38922)	(35971, 42891)	(30227, 40000)	(34283, 44316)
	ESS/S (min, max)	(1.01, 1.37)	(2.68, 3.66)	(3.38, 4.04)	(2.97, 3.93)	(3.36, 4.35)
	ESS/A (min, max)	(0.20, 0.28)	(1.13, 1.54)	(1.42, 1.70)	(1.21, 1.60)	(1.37, 1.78)
δ	ESS (min, max)	(13624, 16678)	(16145, 28401)	(18109, 31180)	(15749, 25582)	(9464, 29271)
	ESS/S (min, max)	(0.93, 1.14)	(1.52, 2.67)	(1.70, 2.93)	(1.55, 2.51)	(0.93, 2.87)
	ESS/A (min, max)	(0.19, 0.23)	(0.64, 1.13)	(0.72, 1.24)	(0.63, 1.02)	(0.38, 1.17)
\mathbf{H}	ESS (min, max)	(12195, 22072)	(35292, 40000)	(46273, 69861)	(33089, 40000)	(43658, 70275)
	ESS/S (min, max)	(0.84, 1.51)	(3.32, 3.76)	(4.35, 6.57)	(3.25, 3.93)	(4.28, 6.90)
	ESS/A (min, max)	(0.17, 0.31)	(1.40, 1.58)	(1.83, 2.77)	(1.33, 1.60)	(1.75, 2.82)
ν	ESS	17797	40000	53388	40000	56313
	ESS/S	1.22	3.76	5.02	3.93	5.53
	ESS/A	0.25	1.58	2.11	1.60	2.26
$\mathbf{z}_{1,\cdot}$	ESS (min, max)	(22130, 24317)	(30533, 40000)	(37065, 70920)	(40000, 40000)	(64787, 68952)
	ESS/S (min, max)	(1.52, 1.67)	(2.87, 3.76)	(3.49, 6.67)	(3.93, 3.93)	(6.36, 6.77)
	ESS/A (min, max)	(0.31, 0.34)	(1.21, 1.58)	(1.47, 2.81)	(1.60, 1.60)	(2.60, 2.76)
$\mathbf{x}_{1,\cdot}$	ESS (min, max)	(22149, 24858)	(27525, 40000)	(33768, 70763)	(40000, 40000)	(63230, 68873)
	ESS/S (min, max)	(1.52, 1.70)	(2.59, 3.76)	(3.18, 6.66)	(3.93, 3.93)	(6.21, 6.76)
	ESS/A (min, max)	(0.31, 0.34)	(1.09, 1.58)	(1.34, 2.80)	(1.60, 1.60)	(2.53, 2.76)

Table 4: Effective sample sizes and computing times for the dynamic inverted Wishart model (26,29). In all cases, the results are based on 10 independent chains/trajectories and reported computing times are the total computing times over these 10 replica. For rstan, default sampler parameters with 1000 warmup transitions followed by 1000 sampling transitions were used. For pdphmc, $T = 5000$ split evenly between warmup and sampling, 1000 samples and an VARI type diagonal mass matrix were applied. Both computing times for the sampling (S) period and for all (A) computations (warmup and sampling) are provided, and ESSes are weighted both for S and A.

where $\boldsymbol{\mu}_g, \boldsymbol{\delta}_g \in (-1, 1), \boldsymbol{\sigma}_g > 0, g = 1, \dots, G$ are parameters.

The joint distribution of parameters $\boldsymbol{\theta} = (\boldsymbol{\mu}, \boldsymbol{\delta}, \boldsymbol{\sigma}, \mathbf{H}_{2:G,1}, \dots, \mathbf{H}_{G,G-1}, \nu)$ and latent variables \mathbf{x} is difficult to sample from, and in order to reduce “funnel” effects, the Laplace-based transport map reformulation of Osmundsen et al. (2021) (without Newton iterations) is used here. For every admissible $\boldsymbol{\theta}$, a smooth bijective mapping, say $\mathbf{x} = \gamma_{\boldsymbol{\theta}}(\mathbf{z}), \mathbf{z} \in \mathbb{R}^{Gn}$, is introduced so that $p(\mathbf{z}, \boldsymbol{\theta} | \mathbf{Y}_{1:n}) \propto |\nabla_{\mathbf{z}} \text{vec}(\gamma_{\boldsymbol{\theta}}(\mathbf{z}))| [p(\mathbf{x}, \boldsymbol{\theta} | \mathbf{Y}_{1:n})]_{\mathbf{x}=\gamma_{\boldsymbol{\theta}}(\mathbf{z})}$ approximates $p(\boldsymbol{\theta} | \mathbf{Y}_{1:n}) \mathcal{N}(\mathbf{z} | \mathbf{0}_{Gn}, \mathbf{I}_{Gn})$. Subsequently, NGRHMC/HMC targeting $p(\mathbf{z}, \boldsymbol{\theta} | \mathbf{Y}_{1:n})$ are performed. The reader is referred Appendix E and Osmundsen et al. (2021) for more details on the construction of $\gamma_{\boldsymbol{\theta}}$ and Appendix E for further details such as priors.

The data considered are $n = 2514$ daily observations of realized covariance matrices for $G = 5$ stocks (American Express, Citigroup, General Electric, Home Depot, IBM) between January 1, 2000 and December 31, 2009. See Golosnoy et al. (2012) for details on how this dataset was constructed from high frequency financial data. For these values of n and G , the model involves $Gn = 12570$ latent variables and $3G + G(G - 1)/2 + 1 = 26$ parameters.

6.2 Results

ESSes and time-weighted ESSes for the parameters, $\mathbf{z}_{1:5,1}$ and $\mathbf{x}_{1:5,1}$ are given in Table 4 for two variants of pdphmc and an rstan benchmark. It is seen that the discretely sampled (D) pdphmc uniformly provides faster sampling performance than rstan. The speedup is in particularly significant when taking all (A) computations into account as rstan uses more than 80% of the computing time in the warmup phase, whereas there is relatively little warmup overhead for pdphmc. For continuously sampled (C) pdphmc the picture is somewhat more mixed with numbers ranging from being on par with rstan ($\boldsymbol{\delta}$, event specification 2) to being up to five times faster (\mathbf{H} , both event specifications). Event specification 2 lead to better worst case performance than event specification 1 in all cases other than for \mathbf{H} . However, the differences are not very large which may be explained by the high dimensionality of the model, and that event specifications 1 and 2 are very similar in this case. Still this observation suggest that it may be possible to gain even more efficiency by developing better adaptive event rate specifications.

Posterior means and standard deviations obtained both from rstan and discretely sampled pdphmc presented in Table 6 in the Appendix show no noteworthy deviations (see also Grothe et al., 2019, Table 5). To conclude, pdphmc is fast and reliable alternative to HMC that also scale well to high-dimensional settings.

7 Discussion

This paper has introduced Numerical Generalized Randomized HMC processes as a new, robust and potentially very efficient alternative to conventional MCMC methods. The presently proposed methodology holds promise to be substantially more trustworthy for complicated real-life problems. This improvement is related to two factors:

- The NGRHMC process is time-irreversible, and the present paper is to the author’s knowledge the among the first attempts to leverage time-irreversible processes to produce general purpose and easy to use MCMC-like samplers that scale to high-dimensional problems. By now, there is substantial evidence (see e.g. discussion on page 387 of Fearnhead et al., 2018) that irreversible processes are superior to conventional reversible alternatives such as HMC. In particular, irreversible methods appear to be more robust to irregular target distributions, as transition can be made without regard to the likelihood of the corresponding reversed transition occurring.
- The proposed implementation of NGRHMC process leverages the mature, and widely used field of numerical integration of ordinary differential equations. Common practice for HMC is choosing a fixed step size low order symplectic method and hoping that regions where this step size is too large for numerical stability is not encountered during the simulation. The proposed methodology, on the other hand, relies on high quality adaptive integrators, which have no such stability problems.

Currently, efficient and robust MCMC computations has been a field dominated by tailor-making to specific applications and a large degree of craftsmanship. Effectively, the two above points reduces such MCMC computations into a more routine task of numerically integrating ordinary differential equations using adaptive/automatic methods.

There scope for substantial further work on NGRHMC-processes beyond the initial developments given here. A, by no means complete, list of possible further research directions related to NGRHMC processes is given in Appendix F.

References

Abraham, M. J., T. Murtola, R. Schulz, S. Páll, J. C. Smith, B. Hess, and E. Lindahl (2015). GROMACS: High performance molecular simulations through multi-level parallelism from laptops to supercomputers. *SoftwareX* 1-2, 19–25.

- Alenlöv, J., A. Doucet, and F. Lindsten (2016). Pseudo-marginal Hamiltonian Monte Carlo. arXiv preprint arXiv:1607.02516.
- Andersen, H. C. (1980). Molecular dynamics simulations at constant pressure and/or temperature. *The Journal of Chemical Physics* 72(4), 2384–2393.
- Betancourt, M. (2016). Identifying the optimal integration time in Hamiltonian Monte Carlo. arXiv:1601.00225.
- Bierkens, J., P. Fearnhead, and G. Roberts (2019, 06). The Zig-Zag process and super-efficient sampling for Bayesian analysis of big data. *Ann. Statist.* 47(3), 1288–1320.
- Bierkens, J., S. Grazi, K. Kamatani, and G. Roberts (2020). The boomerang sampler. arXiv:2006.13777.
- Bou-Rabee, N. and A. Eberle (2020). Couplings for Andersen dynamics. arXiv:2009.14239.
- Bou-Rabee, N. and A. Eberle (2021). Mixing time guarantees for unadjusted hamiltonian monte carlo. arXiv:2105.00887.
- Bou-Rabee, N. and J. M. Sanz-Serna (2017, 08). Randomized Hamiltonian Monte Carlo. *Ann. Appl. Probab.* 27(4), 2159–2194.
- Bou-Rabee, N. and J. M. Sanz-Serna (2018). Geometric integrators and the Hamiltonian Monte Carlo method. *Acta Numerica* 27, 113–206.
- Bou-Rabee, N. and K. Schuh (2020). Convergence of unadjusted Hamiltonian Monte Carlo for mean-field models. arXiv:2009.08735.
- Bouchard-Côté, A., S. J. Vollmer, and A. Doucet (2018). The Bouncy Particle Sampler: A nonreversible rejection-free Markov chain Monte Carlo method. *Journal of the American Statistical Association* 113(522), 855–867.
- Cambanis, S., S. Huang, and G. Simons (1981). On the theory of elliptically contoured distributions. *Journal of Multivariate Analysis* 11(3), 368 – 385.
- Cances, E., F. Legoll, and G. Stoltz (2007, 3). Theoretical and numerical comparison of some sampling methods for molecular dynamics. *ESAIM: Mathematical Modelling and Numerical Analysis* 41, 351–389.
- Carpenter, B., A. Gelman, M. Hoffman, D. Lee, B. Goodrich, M. Betancourt, M. Brubaker, J. Guo, P. Li, and A. Riddell (2017). Stan: A probabilistic programming language. *Journal of Statistical Software* 76(1), 1–32.

- Chen, Z. and S. S. Vempala (2019). Optimal convergence rate of Hamiltonian Monte Carlo for strongly logconcave distributions. In D. Achlioptas and L. A. Végh (Eds.), *Approximation, Randomization, and Combinatorial Optimization. Algorithms and Techniques, APPROX/RANDOM 2019, September 20-22, 2019, Massachusetts Institute of Technology, Cambridge, MA, USA*, Volume 145 of *LIPICs*, pp. 64:1–64:12. Schloss Dagstuhl - Leibniz-Zentrum für Informatik.
- Cheng, X., N. S. Chatterji, P. L. Bartlett, and M. I. Jordan (2018, 06–09 Jul). Underdamped langevin mcmc: A non-asymptotic analysis. In S. Bubeck, V. Perchet, and P. Rigollet (Eds.), *Proceedings of the 31st Conference On Learning Theory*, Volume 75 of *Proceedings of Machine Learning Research*, pp. 300–323. PMLR.
- Chopin, N. and J. Ridgway (2017, 02). Leave Pima Indians alone: Binary regression as a benchmark for Bayesian computation. *Statist. Sci.* 32(1), 64–87.
- Cotter, S., T. House, and F. Pagani (2020). The NuZZ: Numerical ZigZag sampling for general models. arXiv:2003.03636.
- Davis, M. H. A. (1984). Piecewise-deterministic Markov processes: A general class of non-diffusion stochastic models. *Journal of the Royal Statistical Society: Series B (Methodological)* 46(3), 353–376.
- Davis, M. H. A. (1993). *Markov models and optimization*. Chapman & Hall, London.
- Deligiannidis, G., D. Paulin, A. Bouchard-Côté, and A. Doucet (2018). Randomized Hamiltonian Monte Carlo as scaling limit of the bouncy particle sampler and dimension-free convergence rates. arXiv:1808.04299.
- Dormand, J. and P. Prince (1987). Runge-Kutta-Nystrom triples. *Computers & Mathematics with Applications* 13(12), 937 – 949.
- E, W. and D. Li (2008). The Andersen thermostat in molecular dynamics. *Communications on pure and applied mathematics* 61.
- Fang, Y., J. M. Sanz-Serna, and R. D. Skeel (2014). Compressible generalized hybrid Monte Carlo. *The Journal of Chemical Physics* 140(17), 174108.
- Fearnhead, P., J. Bierkens, M. Pollock, and G. O. Roberts (2018, 08). Piecewise deterministic Markov processes for continuous-time monte carlo. *Statist. Sci.* 33(3), 386–412.
- Franco, J. and I. Gómez (2014). Symplectic explicit methods of Runge-Kutta-Nyström type for solving perturbed oscillators. *Journal of Computational and Applied Mathematics* 260, 482–493.

- Gelman, A., J. B. Carlin, H. S. Stern, D. B. Dunson, A. Vehtari, and D. Rubin (2014). *Bayesian Data Analysis* (3 ed.). CRC Press.
- Geyer, C. J. (1992). Practical Markov chain Monte Carlo. *Statistical Science* 7(4), pp. 473–483.
- Girolami, M. and B. Calderhead (2011). Riemann manifold Langevin and Hamiltonian Monte Carlo methods. *Journal of the Royal Statistical Society: Series B (Statistical Methodology)* 73(2), 123–214.
- Goldstein, H., C. Poole, and J. Safko (2002). *Classical Mechanics* (3 ed.). Addison Wesley.
- Golosnoy, V., B. Gribisch, and R. Liesenfeld (2012). The conditional autoregressive wishart model for multivariate stock market volatility. *Journal of Econometrics* 167(1), 211 – 223.
- Grothe, O., T. S. Kleppe, and R. Liesenfeld (2019). The gibbs sampler with particle efficient importance sampling for state-space models. *Econometric Reviews* 38(10), 1152–1175.
- Hairer, E., S. P. Nørsett, and G. Wanner (1993). *Solving Ordinary Differential Equations I (2nd Revised. Ed.): Nonstiff Problems*. Berlin, Heidelberg: Springer-Verlag.
- Hoffman, M. D. and A. Gelman (2014). The no-u-turn sampler: Adaptively setting path lengths in Hamiltonian Monte Carlo. *Journal of Machine Learning Research* 15, 1593–1623.
- Horowitz, A. M. (1991). A generalized guided Monte Carlo algorithm. *Physics Letters B* 268(2), 247–252.
- Kleppe, T. S. (2016). Adaptive step size selection for Hessian-based manifold Langevin samplers. *Scandinavian Journal of Statistics* 43(3), 788–805.
- Kleppe, T. S. (2018). Modified Cholesky Riemann manifold Hamiltonian Monte Carlo: exploiting sparsity for fast sampling of high-dimensional targets. *Statistics and Computing* 28(4), 795–817.
- Kleppe, T. S. (2019). Dynamically rescaled Hamiltonian Monte Carlo for Bayesian hierarchical models. *Journal of Computational and Graphical Statistics* 28(3), 493–507.
- Lee, Y. T., Z. Song, and S. S. Vempala (2018). Algorithmic theory of ODEs and sampling from well-conditioned logconcave densities. arXiv:1812.06243.
- Leimkuhler, B. and C. Matthews (2015). *Molecular Dynamics With Deterministic and Stochastic Numerical Methods*. Springer.
- Leimkuhler, B. and S. Reich (2004). *Simulating Hamiltonian dynamics*. Cambridge University Press.

- Li, D. (2007). On the rate of convergence to equilibrium of the Andersen thermostat in molecular dynamics. *Journal of Statistical Physics* 129.
- Livingstone, S., M. F. Faulkner, and G. O. Roberts (2019, 04). Kinetic energy choice in Hamiltonian/hybrid Monte Carlo. *Biometrika* 106(2), 303–319.
- Lu, J. and L. Wang (2020). On explicit l^2 -convergence rate estimate for piecewise deterministic Markov processes in MCMC algorithms. arXiv:2007.14927.
- Mackenze, P. B. (1989). An improved hybrid Monte Carlo method. *Physics Letters B* 226(3), 369–371.
- Mangoubi, O. and A. Smith (2017). Rapid mixing of Hamiltonian Monte Carlo on strongly log-concave distributions. arXiv:1708.07114.
- Mangoubi, O. and A. Smith (2019). Mixing of hamiltonian monte carlo on strongly log-concave distributions 2: Numerical integrators. In K. Chaudhuri and M. Sugiyama (Eds.), *Proceedings of the Twenty-Second International Conference on Artificial Intelligence and Statistics*, Volume 89 of *Proceedings of Machine Learning Research*, pp. 586–595. PMLR.
- McCullagh, P. and J. A. Nelder (1989). *Generalized Linear Models, 2nd Ed.* New York: Chapman & Hall.
- Michie, D., D. J. Spiegelhalter, and C. C. Taylor (Eds.) (1994). *Machine Learning, Neural and Statistical Classification*. Series in Artificial Intelligence. Hemel Hempstead, Hertfordshire, England: Ellis Horwood.
- Neal, R. M. (2003). Slice sampling. *The Annals of Statistics* 31(3), 705–767.
- Neal, R. M. (2010). MCMC using Hamiltonian dynamics. In *Handbook of Markov Chain Monte Carlo*, pp. 113–162.
- Nishimura, A. and D. Dunson (2020). Recycling Intermediate Steps to Improve Hamiltonian Monte Carlo. *Bayesian Analysis* 15(4), 1087 – 1108.
- Osmundsen, K. K., T. S. Kleppe, and R. Liesenfeld (2021). Importance sampling-based transport map Hamiltonian Monte Carlo for Bayesian hierarchical models. *Journal of Computational and Graphical Statistics forthcoming*.
- Pakman, A. and L. Paninski (2014). Exact Hamiltonian Monte Carlo for truncated multivariate Gaussians. *Journal of Computational and Graphical Statistics* 23(2), 518–542.
- Press, W. H., S. A. Teukolsky, W. T. Vetterling, and B. P. Flannery (2007). *Numerical Recipes 3rd Edition: The Art of Scientific Computing*. Cambridge University Press.

- Robert, C. P. and G. Casella (2004). *Monte Carlo Statistical Methods* (second ed.). Springer.
- Roberts, G. O. and J. S. Rosenthal (1998). Optimal scaling of discrete approximations to Langevin diffusions. *Journal of the Royal Statistical Society: Series B (Statistical Methodology)* 60(1), 255–268.
- Sanz-Serna, J. and M. Calvo (1994). *Numerical Hamiltonian Problems*. Dover Publications Inc, New York.
- Stan Development Team (2017). Stan modeling language users guide and reference manual, version 2.17.0.
- Vanetti, P., A. Bouchard-Côté, G. Deligiannidis, and A. Doucet (2018). Piecewise-deterministic Markov chain Monte Carlo. arXiv:1707.05296v2.
- Welling, M. and Y. W. Teh (2011). Bayesian learning via stochastic gradient Langevin dynamics. In *Proceedings of the 28th International Conference on International Conference on Machine Learning*, Madison, WI, USA, pp. 681–688. Omnipress.
- Wu, C., J. Stoehr, and C. P. Robert (2018). Faster Hamiltonian Monte Carlo by learning leapfrog scale. arXiv:1810.04449.

Online Appendix to “Connecting the Dots: Numerical Randomized Hamiltonian Monte Carlo with State-Dependent Event Rates” by Tore Seland Kleppe

This version: February 1, 2022

In this online Appendix, equation numbers ≤ 29 refer to equations in the main article text.

A Details of derivations

A.1 The left-hand side of (5) is the Poisson bracket between p and \mathcal{H}

Suppose $D = 2d$, $\mathbf{z} = [\mathbf{q}^T, \mathbf{p}^T]^T$ and $\Phi(\mathbf{z})$ corresponds to Hamilton’s equations associated with separable Hamiltonian (1), i.e.

$$\Phi(\mathbf{z}) = \begin{bmatrix} \mathbf{M}^{-1}\mathbf{p} \\ \nabla_{\mathbf{q}} \log \tilde{\pi}(\mathbf{q}) \end{bmatrix} = \mathbf{J} \nabla_{\mathbf{z}} \mathcal{H}(\mathbf{z}), \quad \mathbf{J} = \begin{bmatrix} \mathbf{0}_{d,d} & \mathbf{I}_d \\ -\mathbf{I}_d & \mathbf{0}_{d,d} \end{bmatrix},$$

Then the left-hand side of the stationary Fokker-Planck equation (5) is equal to the Poisson Bracket $\{p, \mathcal{H}\}(\mathbf{z})$ (see e.g. Leimkuhler and Reich, 2004, Section 3.3) between the density $p(\mathbf{z})$ and the Hamiltonian $\mathcal{H}(\mathbf{z})$, namely

$$\begin{aligned} \{p, \mathcal{H}\}(\mathbf{z}) &:= [\nabla_{\mathbf{z}} p(\mathbf{z})]^T \mathbf{J} \nabla_{\mathbf{z}} \mathcal{H}(\mathbf{z}), \\ &= [\nabla_{\mathbf{q}} p(\mathbf{z})]^T \mathbf{M}^{-1} \mathbf{p} + [\nabla_{\mathbf{p}} p(\mathbf{z})]^T \nabla_{\mathbf{q}} \log \tilde{\pi}(\mathbf{q}), \\ &= \sum_{i=1}^d \frac{\partial}{\partial q_i} [\mathbf{M}^{-1} \mathbf{p}]_i p(\mathbf{z}) + \sum_{i=1}^d \frac{\partial}{\partial p_i} [\nabla_{\mathbf{q}} \log \tilde{\pi}(\mathbf{q})]_i p(\mathbf{z}), \\ &= \sum_{i=1}^D \frac{\partial}{\partial z_i} [\Phi_i(\mathbf{z}) p(\mathbf{z})]. \end{aligned}$$

For any first integral, say $g(\mathbf{z})$ (i.e. conserved quantity so that $g(\varphi_t(\mathbf{z})) = g(\mathbf{z}) \forall t, \mathbf{z}$), the Poisson bracket between g and \mathcal{H} is zero for all \mathbf{z} . Clearly, the BG distribution $\rho(\mathbf{z}) \propto \exp(-\mathcal{H}(\mathbf{z}))$ is a first integral of \mathcal{H} , and hence $\{\mathcal{H}, \rho\}(\mathbf{z}) = \sum_{i=1}^D \frac{\partial}{\partial z_i} [\Phi_i(\mathbf{z}) \rho(\mathbf{z})] = 0 \forall \mathbf{z}$.

Note also that the same argument goes through for a general separable Hamiltonian, say $\mathcal{H}(\mathbf{z}) = -\nabla_{\mathbf{q}} \log \tilde{\pi}(\mathbf{q}) + V(\mathbf{p})$, with $\Phi(\mathbf{z}) = [\nabla_{\mathbf{p}} V(\mathbf{p})^T, \nabla_{\mathbf{q}} \log \tilde{\pi}(\mathbf{q})]$.

A.2 General Markov kernel momentum refreshes

Given some event rate $\lambda(\mathbf{q}, \mathbf{p}) > 0$ so that $C(\mathbf{q}) = \int \mathcal{N}(\mathbf{p}|\mathbf{0}_d, \mathbf{M})\lambda(\mathbf{q}, \mathbf{p})d\mathbf{p} < \infty$ for each admissible \mathbf{q} . Define the conditional density

$$v_{\mathbf{q}}(\mathbf{p}) = \frac{\mathcal{N}(\mathbf{p}|\mathbf{0}_d, \mathbf{M})\lambda(\mathbf{q}, \mathbf{p})}{C(\mathbf{q})},$$

and, for each fixed \mathbf{q} , let $K_{\mathbf{q}}(\mathbf{p}|\mathbf{p}')$ be the density of a Markov kernel that leaves $v_{\mathbf{q}}(\mathbf{p})$ invariant, i.e.

$$\int K_{\mathbf{q}}(\mathbf{p}|\mathbf{p}')v_{\mathbf{q}}(\mathbf{p}')d\mathbf{p}' = v_{\mathbf{q}}(\mathbf{p}).$$

Then, take the transition distribution at events to be

$$Q(\mathbf{z}|\mathbf{z}') = \delta(\mathbf{q} - \mathbf{q}')K_{\mathbf{q}'}(\mathbf{p}|\mathbf{p}'). \quad (30)$$

Under this event specification, the right-hand side of (5) (with $p(\mathbf{z}) = \rho(\mathbf{z})$) reduces to

$$\begin{aligned} & \int \pi(\mathbf{q}')\mathcal{N}(\mathbf{p}'|\mathbf{0}_d, \mathbf{M})\lambda(\mathbf{q}', \mathbf{p}')\delta(\mathbf{q} - \mathbf{q}')K_{\mathbf{q}'}(\mathbf{p}|\mathbf{p}')d\mathbf{z}' - \rho(\mathbf{z})\lambda(\mathbf{z}), \\ & = \pi(\mathbf{q}) \int \mathcal{N}(\mathbf{p}'|\mathbf{0}_d, \mathbf{M})\lambda(\mathbf{q}, \mathbf{p}')K_{\mathbf{q}}(\mathbf{p}|\mathbf{p}')d\mathbf{p}' - \rho(\mathbf{z})\lambda(\mathbf{z}), \\ & = \pi(\mathbf{q})C(\mathbf{q}) \int K_{\mathbf{q}}(\mathbf{p}|\mathbf{p}')v_{\mathbf{q}}(\mathbf{p}')d\mathbf{p}' - \rho(\mathbf{z})\lambda(\mathbf{z}), \\ & = \pi(\mathbf{q})C(\mathbf{q})v_{\mathbf{q}}(\mathbf{p}) - \rho(\mathbf{z})\lambda(\mathbf{z}), \\ & = \pi(\mathbf{q})\mathcal{N}(\mathbf{p}|\mathbf{0}_d, \mathbf{M})\lambda(\mathbf{q}, \mathbf{p}) - \rho(\mathbf{z})\lambda(\mathbf{z}) = 0. \end{aligned}$$

I.e. provided the deterministic dynamics is Hamiltonian as described, the PDMP the process with general event rate $\lambda(\mathbf{q}, \mathbf{p})$ and transition distribution at events (30) admit $\rho(\mathbf{z})$ as a stationary distribution. Note also that the above argument may be modified to accommodate a general \mathbf{p} -marginal of the BG distribution.

A.3 Riemann manifold variants

This section gives the relevant details for constructing continuous time Riemann manifold HMC processes. Such processes rely on selecting a symmetric positive definite “metric tensor” $\mathbf{G}(\mathbf{q}) \in \mathbb{R}^{d \times d}$ which should reflect the “local” precision of the target distribution around \mathbf{q} . The non-separable Hamiltonian \mathcal{K} typically used in such situations is given by (Girolami and Calderhead, 2011)

$$\mathcal{K}(\mathbf{z}) = -\log \tilde{\pi}(\mathbf{q}) + \frac{1}{2} \log(|\mathbf{G}(\mathbf{q})|) + \frac{1}{2} \mathbf{p}^T \mathbf{G}(\mathbf{q})^{-1} \mathbf{p}.$$

Hamilton's equations are still given by

$$\Phi(\mathbf{z}) = \mathbf{J}\nabla_{\mathbf{z}}\mathcal{K}(\mathbf{z}) = \begin{bmatrix} \nabla_{\mathbf{p}}\mathcal{K}(\mathbf{z}) \\ -\nabla_{\mathbf{q}}\mathcal{K}(\mathbf{z}) \end{bmatrix},$$

and BG distribution by $\rho(\mathbf{z}) = \pi(\mathbf{q})\mathcal{N}(\mathbf{p}|\mathbf{0}, \mathbf{G}(\mathbf{q})) = \exp(-\mathcal{K}(\mathbf{z}))W^{-1}$, $W = \int \exp(-\mathcal{K}(\mathbf{z}))d\mathbf{z}$. In terms of numerical implementation, it is seen that Hamilton's equations cannot in this case be reduced to a second order ODE but may still be solved using general purpose first order ODE solvers such as Runge-Kutta methods. A drawback of general Riemann manifold HMC methods is that symplectic integrators for non-separable Hamiltonians are necessary implicit, and hence require many evaluations of Φ per integration step. A pro of the proposed methodology is that adaptive explicit solvers may be used.

The strategy for showing that the drift term in the Fokker-Planck equation (5) vanishes also with Hamiltonian \mathcal{K} is to look directly at the drift term with $p = \rho$. In this case

$$\begin{aligned} \sum_{i=1}^D \frac{\partial}{\partial z_i} [\Phi_i \rho(\mathbf{z})] &= W^{-1} \sum_{i=1}^d \frac{\partial}{\partial q_i} \left[\exp(-\mathcal{K}(\mathbf{z})) \frac{\partial}{\partial p_i} \mathcal{K}(\mathbf{z}) \right] \\ &\quad - W^{-1} \sum_{i=1}^d \frac{\partial}{\partial p_i} \left[\exp(-\mathcal{K}(\mathbf{z})) \frac{\partial}{\partial q_i} \mathcal{K}(\mathbf{z}) \right], \\ &= -\rho(\mathbf{z}) \sum_{i=1}^d \left[\frac{\partial}{\partial q_i} \mathcal{K}(\mathbf{z}) \right] \left[\frac{\partial}{\partial p_i} \mathcal{K}(\mathbf{z}) \right] \\ &\quad + \rho(\mathbf{z}) \sum_{i=1}^d \frac{\partial^2}{\partial q_i \partial p_i} \mathcal{K}(\mathbf{z}) \\ &\quad + \rho(\mathbf{z}) \sum_{i=1}^d \left[\frac{\partial}{\partial p_i} \mathcal{K}(\mathbf{z}) \right] \left[\frac{\partial}{\partial q_i} \mathcal{K}(\mathbf{z}) \right] \\ &\quad - \rho(\mathbf{z}) \sum_{i=1}^d \frac{\partial^2}{\partial p_i \partial q_i} \mathcal{K}(\mathbf{z}), \\ &= 0. \end{aligned}$$

(For clarity; the second equality is based on the chain rule $\frac{\partial}{\partial z_i} \exp(-\mathcal{K}(\mathbf{z}))\Phi_i(\mathbf{z}) = -\exp(-\mathcal{K}(\mathbf{z}))\Phi_i(\mathbf{z})\frac{\partial}{\partial z_i}\mathcal{K}(\mathbf{z}) + \exp(-\mathcal{K}(\mathbf{z}))\frac{\partial}{\partial z_i}\Phi_i(\mathbf{z})$).

As also the flow associated with \mathcal{K} preserves the BG distribution, one is also in this case free to choose the event specification solely on making the right-hand side of (5) vanish. Essentially the same event specification cases as in the separable case, with minimal modifications to account for the position-dependence in the BG

distribution \mathbf{p} -marginal, applies. I.e.

$$\lambda(\mathbf{z}) = \omega(\mathbf{q}), \quad Q(\mathbf{p}|\mathbf{z}') = \mathcal{N}(\mathbf{p}|\phi\mathbf{p}', \sqrt{1-\phi^2}\mathbf{G}(\mathbf{q}')),$$

and

$$\lambda(\mathbf{z}) = \lambda(\mathbf{q}, \mathbf{p}), \quad Q(\mathbf{p}|\mathbf{z}') \propto \lambda(\mathbf{q}', \mathbf{p})\mathcal{N}(\mathbf{p}|\mathbf{0}_d, \mathbf{G}(\mathbf{q}')),$$

lead to on target processes. The arguments leading to this conclusion are analogous to those in Appendix A.2 and are not repeated.

A.4 Langevin limit

To obtain the Langevin limit under event specification 1, consider first a large, but finite λ , and condition on a sequence of inter-event times $\tau_i \sim \text{iid } \text{Exp}(\lambda^{-1})$ $i = 1, 2, \dots$. A time-discretized version of the PDMP \mathcal{Z}_t , say $\tilde{\mathbf{z}}_j = [\tilde{\mathbf{q}}_j^T, \tilde{\mathbf{p}}_j^T]^T \approx \mathcal{Z}_{\sum_{i=1}^j \tau_i}$, obtains by first applying a single leap-frog step (with time step τ_i) to each deterministic transition to get the state immediately before the $(i+1)$ th event, say $\tilde{\mathbf{z}}_{i+1}^*$:

$$\tilde{\mathbf{p}}_{i+1/2} = \tilde{\mathbf{p}}_i + \frac{\tau_{i+1}}{2} \nabla_{\mathbf{q}} \log \tilde{\pi}(\tilde{\mathbf{q}}_i), \quad (31)$$

$$\tilde{\mathbf{q}}_{i+1}^* = \tilde{\mathbf{q}}_i + \tau_{i+1} \mathbf{M}^{-1} \tilde{\mathbf{p}}_{i+1/2}, \quad (32)$$

$$\tilde{\mathbf{p}}_{i+1}^* = \tilde{\mathbf{p}}_{i+1/2} + \frac{\tau_{i+1}}{2} \nabla_{\mathbf{q}} \log \tilde{\pi}(\tilde{\mathbf{q}}_{i+1}^*).$$

(the latter equation is not needed but is given for completeness of the leapfrog step). Secondly, at the event (at time $\sum_{j=1}^{i+1} \tau_j$) $\tilde{\mathbf{z}}_{i+1}$ is sampled according to $Q(\cdot|\tilde{\mathbf{z}}_{i+1}^*)$, which reduces to:

$$\tilde{\mathbf{q}}_{i+1} = \tilde{\mathbf{q}}_{i+1}^* \quad (33)$$

$$\tilde{\mathbf{p}}_{i+1} = \varepsilon_{i+1}, \quad \varepsilon_{i+1} \sim \text{iid } N(\mathbf{0}_{d,1}, \mathbf{M}). \quad (34)$$

Now, since the time-discrete momentum is resampled each step, the discrete time (marginal) position dynamics $\tilde{\mathbf{q}}_i$ obtains by combining (31,33) and time-shifted (34) into (32):

$$\tilde{\mathbf{q}}_{i+1} = \tilde{\mathbf{q}}_i + \frac{\tau_{i+1}^2}{2} \mathbf{M}^{-1} \nabla_{\mathbf{q}} \log \tilde{\pi}(\tilde{\mathbf{q}}_i) + \tau_i \mathbf{M}^{-\frac{1}{2}} \eta_i, \quad (35)$$

where $\eta_i = \mathbf{M}^{-\frac{1}{2}} \varepsilon_i \sim N(\mathbf{0}_{d,1}, \mathbf{I}_d)$. Equation 35 is recognized to be the Euler-Maruyama discretization of (12) with time step size τ_{i+1}^2 . Finally, upon letting $\lambda \rightarrow \infty$, the discrete time process $\tilde{\mathbf{z}}_j$ converges to the underlying PDMP, and $\tilde{\mathbf{q}}_j$ to the Langevin process (12) a.s.

A.5 Arc-length and event specification 2

Consider the calculation of the arc-length of some (position) dynamics $\mathbf{q}(s)$, $s \in [0, t]$ using the distance

$$d(\mathbf{q}, \mathbf{q}') = \sqrt{(\mathbf{q} - \mathbf{q}')^T \mathbf{M} (\mathbf{q} - \mathbf{q}')}$$

Notice that throughout this text, \mathbf{M}^{-1} should reflect $Var(\mathbf{q})$ and hence the distance d aims at making the contribution of each dimension more uniform. Discretizing time $s_i = i\Delta$, $\Delta = t/N$, the arc-length may be arbitrarily well approximated by

$$\begin{aligned} A_N &= \sum_{i=1}^N \sqrt{(\mathbf{q}(s_i) - \mathbf{q}(s_{i-1}))^T \mathbf{M} (\mathbf{q}(s_i) - \mathbf{q}(s_{i-1}))}, \\ &= \sum_{i=1}^N \Delta \sqrt{\left[\frac{\mathbf{q}(s_i) - \mathbf{q}(s_{i-1})}{\Delta} \right]^T \mathbf{M} \left[\frac{\mathbf{q}(s_i) - \mathbf{q}(s_{i-1})}{\Delta} \right]}, \end{aligned}$$

for large N . Letting $N \rightarrow \infty$ one obtains by a standard limit argument that

$$A_N \rightarrow A = \int_0^t \sqrt{[\dot{\mathbf{q}}(s)]^T \mathbf{M} \dot{\mathbf{q}}(s)} ds.$$

Finally, from the first of Hamilton's equations, $\dot{\mathbf{q}}(s) = \mathbf{M}^{-1} \mathbf{p}(s)$:

$$A = \int \sqrt{\mathbf{p}(s)^T \mathbf{M}^{-1} \mathbf{p}(s)} ds$$

which is (up to a multiplicative constant) the integrated $\lambda(\mathbf{z})$ (4) used in event specification 2.

B Temporal averages of the Hamiltonian dynamics for Gaussian targets

This section considers the temporal average of the flow for *Gaussian* targets. In particular it is shown that exploring only a single energy levelset is sufficient to get asymptotically correct estimates for any linear combination of the mean of the target when continuous sampling is employed.

Consider a $N(\mu, \Sigma)$ target distribution, where Σ is positive definite and finite. The Hamiltonian dynamics $\mathbf{z}(t)$ is then the solution to the linear differential equation

$$\dot{\mathbf{z}}(t) = \mathbf{B}\mathbf{z}(t) + \mathbf{b} \tag{36}$$

where

$$\mathbf{B} = \begin{bmatrix} \mathbf{0}_{d,d} & \mathbf{M}^{-1} \\ -\Sigma^{-1} & \mathbf{0}_{d,d} \end{bmatrix}, \quad \mathbf{b} = \begin{bmatrix} \mathbf{0}_{d,1} \\ \Sigma^{-1}\mu \end{bmatrix}.$$

Consider first the case where $\mu = \mathbf{0}_d$, which results in the solution to (36) given by $\mathbf{z}(t) = \exp(t\mathbf{B})\mathbf{z}(0)$ where $\exp(t\mathbf{B})$ is the matrix exponential of matrix $t\mathbf{B}$. This solution necessarily conserves the associated Hamiltonian, which may be written as

$$\mathcal{H}(\mathbf{z}(t)) = \frac{1}{2}\mathbf{z}(t)^T \mathbf{B}^* \mathbf{z}(t), \quad \mathbf{B}^* = \begin{bmatrix} \Sigma^{-1} & \mathbf{0}_{d,d} \\ \mathbf{0}_{d,d} & \mathbf{M}^{-1} \end{bmatrix}. \quad (37)$$

From the conservation of (37), it is clear that the solutions $\mathbf{z}(t)$ are restricted to an ellipsoid (centered in $\mathbf{0}_{2d,1}$) in \mathbb{R}^{2d} , and hence $\exp(t\mathbf{B})\mathbf{v} = O(1)$ as $t \rightarrow \infty$ for any finite vector $\mathbf{v} \in \mathbb{R}^{2d}$.

Now, consider the general $\mu \in \mathbb{R}^d$ case. Any linear algebra textbook provides the solution to (36), in terms of an initial state $\mathbf{z}(0)$, namely

$$\mathbf{z}(t) = \exp(t\mathbf{B})\mathbf{z}(0) + \mathbf{B}^{-1}[\exp(t\mathbf{B}) - \mathbf{I}_{2d}]\mathbf{b}.$$

Suppose now that we seek the temporal average of some linear combination, say $\mathbf{Kz}(t)$, $\mathbf{K} \in \mathbb{R}^{l \times 2d}$, of the dynamics:

$$\begin{aligned} \frac{1}{T} \int_0^T \mathbf{Kz}(t) dt &= \frac{1}{T} \mathbf{K} \left[\int_0^T \exp(t\mathbf{B}) dt \right] \mathbf{z}(0) + \frac{1}{T} \mathbf{KB}^{-1} \left[\int_0^T \exp(t\mathbf{B}) dt \right] \mathbf{b} - \mathbf{KB}^{-1}\mathbf{b} \\ &= \frac{1}{T} \mathbf{KB}^{-1} [\exp(T\mathbf{B}) - \mathbf{I}_{2d}] \mathbf{z}(0) \\ &\quad + \frac{1}{T} \mathbf{KB}^{-1} \mathbf{B}^{-1} [\exp(T\mathbf{B}) - \mathbf{I}_{2d}] \mathbf{b} \\ &\quad + \mathbf{K}[\mu^T, \mathbf{0}_{d,1}^T]^T. \end{aligned}$$

Now, former two terms in the latter representation of $\frac{1}{T} \int_0^T \mathbf{Kz}(t) dt$ vanishes as $T \rightarrow \infty$, (since $\mathbf{KB}^{-1}[\exp(T\mathbf{B}) - \mathbf{I}_{2d}]\mathbf{z}(0) = O(1)$ and $\mathbf{KB}^{-1}\mathbf{B}^{-1}[\exp(T\mathbf{B}) - \mathbf{I}_{2d}]\mathbf{b} = O(1)$), and one may conclude that

$$\frac{1}{T} \int_0^T \mathbf{Kz}(t) dt \xrightarrow{T \rightarrow \infty} \mathbf{K} \begin{bmatrix} \mu \\ \mathbf{0}_{d,1} \end{bmatrix},$$

invariantly of $\mathbf{z}(0)$ (or equivalently the energy level set $\mathbf{z}(t)$ is restricted to).

For the interested reader; a further special case obtains when the mass matrix is chosen to be the precision

of the target, i.e. $\mathbf{M} = \Sigma^{-1}$. Then the centered flow takes a particularly simple form:

$$\exp(t\mathbf{B}) = \begin{bmatrix} \cos(t)\mathbf{I}_{d,d} & \sin(t)\Sigma \\ -\sin(t)\Sigma & \cos(t)\mathbf{I}_{d,d} \end{bmatrix}.$$

(This latter expression obtains from that even powers of \mathbf{B} are $\pm\mathbf{I}_{2d}$ and odd powers of \mathbf{B} are $\pm\mathbf{B}$, and subsequently employing this information in infinite series defining $\exp(t\mathbf{B})$.) In this case, the former two terms in the latter representation of $\frac{1}{T} \int_0^T \mathbf{K}\mathbf{z}(t)dt$ above vanishes whenever $t = 2\pi k$, k is an integer. I.e. the trajectory forms exactly k closed orbits centered in μ on the underlying ellipsoid, and the average then becomes μ . For $\mathbf{M} \neq \Sigma^{-1}$, the time T_i required for $T_i^{-1} \int_0^{T_i} q_i(t)dt = \mu_i$ generally depends on i , and thus only the asymptotic result above holds in this case.

C Details related to numerical implementation

Denote by ψ_ε the RKN step. Then $\hat{\mathbf{s}}(\tau + \varepsilon) = \psi_\varepsilon(\mathbf{s}(\tau))$, starting at $\mathbf{s}(\tau)$ and with time step size ε , is a 6th order approximation of the flow. In addition, when ψ_ε has been evaluated, the following is available at negligible additional cost (in particular no further evaluations of the right-hand side of (17)):

1. A 4th order approximation, say $\tilde{\mathbf{s}}(\tau + \varepsilon)$, of $\mathbf{s}(\tau + \varepsilon)$ used for estimation of the (local) error incurred, which is subsequently used in the adaptive step size selection.
2. A 6th order interpolation approximation, say $\hat{\mathbf{s}}(\tau + \xi\varepsilon)$, of any element of $(\mathbf{q}(\tau + \xi\varepsilon), \dot{\mathbf{q}}(\tau + \xi\varepsilon), \mathbf{r}(\tau + \xi\varepsilon))$, $\xi \in (0, 1)$.

A fairly standard PI-step size controller (see e.g. Press et al., 2007, Section 17.2.1) was used to select ε dynamically, by maintaining that

$$\max_i \frac{|\hat{\mathbf{s}}_i(\tau + \varepsilon) - \tilde{\mathbf{s}}_i(\tau + \varepsilon)|}{tol_a + tol_r |\hat{\mathbf{s}}_i(\tau + \varepsilon)|} < 1$$

for all time RKN steps. Here, tol_a and tol_r are the absolute- and relative error tolerances respectively, which must be chosen a-priori.

A quite general outline of the numerical algorithm for simulating NGRHMC processes is given in Algorithm 1. The outlined algorithm produces both integrated moments approximating $\int g_k(\mathbf{q})\pi(\mathbf{q})d\mathbf{q}$, $k = 1, \dots, m$ based on (7) and discrete time samples \mathbf{S} . Notice that Algorithm 1 assumes event intensities not depending on the momentum coordinate. However, it is straight forward to extend to the Algorithm to account for momentum-dependent event-rates based on the interpolation option of the RKN step.

Algorithm 1 Basic NGRHMC algorithm based on modified RKN integrator. Notice, this formulation assumes that the event intensity λ depends on \mathbf{q} only. The algorithm produces both continuous time estimates (7) of the given moments, and discrete time samples \mathbf{S} which may be used similarly to conventional MCMC samples.

Input: Target log-density kernel $\log \tilde{\pi}(\mathbf{q})$, $\mathbf{q} \in \mathbb{R}^d$ associated with target density $\pi(\mathbf{q})$.
Input: Event specification (λ, Q) (see e.g. Table 1).
Input: Mass matrix $\mathbf{M} \in \mathbb{R}^{d \times d}$, symmetric, positive definite (e.g. $\mathbf{M} = \mathbf{I}_d$).
Input: Simulation time span $T \in \mathbb{R}^+$.
Input: Number of discrete time samples N .
Input: Initial position $\mathbf{q}_0 \in \mathbb{R}^d$.
Input: Numerical error tolerances tol_a, tol_r (e.g. $tol_a = tol_r = 1.0e - 3$).
Input: Moments $g_1, \dots, g_m, g_k : \mathbb{R}^d \mapsto \mathbb{R}$, $k = 1, \dots, m$, for which $\int g_k(\mathbf{q})\pi(\mathbf{q})d\mathbf{q}$ are to be estimated.

Define integrated quantities $\mathcal{M}(\mathbf{q}) = [\lambda(\mathbf{q}), g_1(\mathbf{q}), \dots, g_m(\mathbf{q})] : \mathbb{R}^d \mapsto \mathbb{R}^{m+1}$.

```

t ← 0,                                     ▷ Continuous time process time.
Q(0) ← q0.                               ▷ Initial q configuration.
P(0) ~ N(0d, M).                          ▷ Initial p configuration (in case of autocorrelated momentum refreshes)
g ← 0m                                    ▷ Storage for estimated moments.
S ← 0d,M                                  ▷ Storage for discrete time samples.
i ← 1                                       ▷ Discrete samples counter.
while t < T do                               ▷ Main loop over events
  P(t) ~ Q(·|Z(t-)).                       ▷ Simulate new momentum
  u ~ Exp(1).                               ▷ See equation 4
  ŝ(0) ← (Q(t), M-1P(t), 0m+1).          ▷ Initial conditions for system of ODEs (17)
  τ ← 0.                                    ▷ Hamiltonian dynamics (between-events) time.
  while ŝ2d+1(τ) < u and t + τ < T do
    Propose a new step size ε.              ▷ Recall ŝ2d+1(τ) ≈ ∫0τ λ(q(v))dv
    ε ← min(ε, T - (t + τ))                ▷ Using e.g. PI step size controller.
    ŝ(τ + ε) = ψε(ŝ(τ)) for ODE (17)      ▷ No simulation beyond process time t = T.
    ξ ← 1                                   ▷ The RKN step
    if ŝ2d+1(τ + ε) > u then                ▷ "If(event occurred during this integration step)"
      Find ξ so that ŝ2d+1(τ + ξε) = u    ▷ Time between-events was τ + ξε.
    end if
    Q(t + τ + r) ← ŝ1:d(τ + r), r ∈ [0, ξε] ▷ Position q.
    P(t + τ + r) ← Mŝd+1:2d(τ + r), r ∈ [0, ξε] ▷ Momentum p.
    while τ + ξε ≥ iT/N do                  ▷ The ith sample during current integration step?
      S1:d,i ← Q(iT/N)                    ▷ Collect sample (in practice done using RKN step interpolation).
      i ← i + 1                             ▷ Advance discrete time samples counter.
    end while
    τ ← τ + ε                               ▷ Update Hamiltonian dynamics time
  end while                                 ▷ Hamiltonian dynamics integration loop
  t ← t + (τ - ε) + ξε.                    ▷ Update process time t
  g ← g + ŝ2d+2:2d+1+m((τ - ε) + ξε)     ▷ t-1g estimates moments
end while                                  ▷ Event loop

Return T-1g                               ▷ T-1gk → ∫ gk(q)π(q)dq as T → ∞.
Return S.   ▷ The columns of S are dependent random draws whose marginal distribution approaches π(q).

```

D The salamander mating data using crossed random effects

For the purpose of further benchmarking of the proposed methodology against rstan, this section considers a crossed random effects model for the Salamander mating data of McCullagh and Nelder (1989, chap 14.5). The formulation of the model is an example model for INLA (see Salamander Model B at <http://www.r-inla.org/examples/volume-ii>), the particular parameterization is taken from Kleppe (2019, Section 5.3, "Full CIP/DRHMC") and the rstan implementation is identical to that of Kleppe (2019). The model is characterized by random effects precision priors

$$\tau_F \sim \text{Gamma}(1, 0.622), \tau_M \sim \text{Gamma}(1, 0.622),$$

$$\mathbf{P}_F \sim \text{Wishart}_2(3.0, \mathbf{W}), \mathbf{P}_M \sim \text{Wishart}_2(3.0, \mathbf{W}), \mathbf{W} = \text{diag}(0.804, 0.804),$$

random effects

$$[\mathbf{b}_{i1}^F, \mathbf{b}_{i2}^F]^T \sim \text{iid } N(\mathbf{0}_2, \mathbf{P}_F^{-1}), i = 1, \dots, 20, \quad (38)$$

$$[\mathbf{b}_{j1}^M, \mathbf{b}_{j2}^M]^T \sim \text{iid } N(\mathbf{0}_2, \mathbf{P}_M^{-1}), j = 1, \dots, 20, \quad (39)$$

$$\mathbf{b}_{i3}^F \sim \text{iid } N(0, \tau_F^{-1}), i = 1, \dots, 20,$$

$$\mathbf{b}_{j3}^M \sim \text{iid } N(0, \tau_M^{-1}), j = 1, \dots, 20,$$

and finally the observation equation

$$\mathbf{y}_{ijk} | \mathbf{\Pi}_{ijk} \sim \text{Bernoulli}(\mathbf{\Pi}_{ijk}), \text{logit}(\mathbf{\Pi}_{ijk}) = \mathbf{x}_{ijk}^T \beta + \mathbf{b}_{ik}^F + \mathbf{b}_{jk}^M.$$

The observations are coded as 1 for successful mating of female salamander i and male salamander j in experiment $k = 1, 2, 3$. The salamanders in experiment $k = 1, 2$ are identical, and therefore their associated random effects (38,39) are allowed to be correlated. Finally, $\mathbf{x}_{ijk} \in \mathbb{R}^5$ is a covariate vector and $\beta \in \mathbb{R}^5$ is a fixed effect with flat prior. Experiment outcomes were recorded in 360 combinations of i, j, k .

Details on the parameterization of model, aiming at making the target distribution suitable for HMC sampling by reducing “funnel” effects, are given in Kleppe (2019). Still the target distribution is quite far from being Gaussian. In total, the model involves $d = 133$ free parameters and random effects to be sampled.

Table 5 provides results, focusing on the posterior marginal precisions and correlations of random effects, as these are typically rather difficult to estimate using MCMC. The overall picture from the experiment is that pdphmc is slightly more efficient than rstan.

	sampling	Prec(\mathbf{b}_{i1}^F)	Prec(\mathbf{b}_{i2}^F)	corr($\mathbf{b}_{i1}^F, \mathbf{b}_{i2}^F$)	Prec(\mathbf{b}_{i1}^M)	Prec(\mathbf{b}_{i2}^M)	corr($\mathbf{b}_{i1}^M, \mathbf{b}_{i2}^M$)	τ_F	τ_M	\mathbf{b}_{\cdot}	β
rstan, total sampling CPU time: 23.43 s (max $\hat{R} = 1.005$)											
post. mean		1.09	0.95	-0.08	1.55	1.11	0.63	2.19	0.74		
post. sd		0.94	0.79	0.40	1.20	0.89	0.26	1.51	0.59		
ESS/CPU time		241	217	103	194	226	137	356	235	≥ 243	≥ 178
pdphmc, event specification 1, $\gamma = 3$, total CPU time: 15.19 s (max $\hat{R} = 1.010$)											
post. mean	D	1.07	0.92	-0.09	1.52	1.09	0.64	2.13	0.68		
post. sd	D	0.91	0.77	0.40	1.18	0.84	0.26	1.52	0.49		
ESS/CPU time	D	149	188	155	274	244	200	333	252	≥ 319	≥ 191
ESS/CPU time	C	137	145	155	246	156	201	352	159	≥ 339	≥ 198
pdphmc, event specification 1, $\gamma = 10.0$, total CPU time: 14.91 s (max $\hat{R} = 1.015$)											
post. mean	D	1.08	0.91	-0.08	1.55	1.12	0.62	2.25	0.74		
post. sd	D	0.91	0.75	0.40	1.21	0.91	0.26	1.56	0.55		
ESS/CPU time	D	244	316	164	339	313	206	344	320	≥ 326	≥ 215
ESS/CPU time	C	142	326	164	355	321	207	365	329	≥ 347	≥ 224
pdphmc, event specification 2, $\gamma = 3.0$, total CPU time: 14.69 s (max $\hat{R} = 1.014$)											
post. mean	D	1.09	0.91	-0.08	1.55	1.13	0.63	2.14	0.73		
post. sd	D	0.91	0.74	0.40	1.17	0.89	0.26	1.50	0.56		
ESS/CPU time	D	265	279	160	246	316	209	339	189	≥ 330	≥ 204
ESS/CPU time	C	208	186	161	221	250	210	357	128	≥ 352	≥ 209
pdphmc, event specification 2, $\gamma = 10.0$, total CPU time: 15.25 s (max $\hat{R} = 1.018$)											
post. mean	D	1.09	0.93	-0.08	1.53	1.13	0.62	2.22	0.71		
post. sd	D	0.90	0.77	0.40	1.15	0.88	0.27	1.59	0.54		
ESS/CPU time	D	270	318	159	322	297	198	338	310	≥ 321	≥ 208
ESS/CPU time	C	198	327	159	271	254	200	359	132	≥ 342	≥ 216

Table 5: Results for the Salamander mating experiment. The table gives posterior means (post. mean), posterior standard deviations (post. sd.), and also the number of effective samples produced per second of computing time (ESS/CPU time). For rstan, the results are based on 10 independent chains with 1000 transitions proceeding 1000 warmup transitions. For pdphmc, the results are based on trajectories of length $T = 2,000$ with the first half discarded as warmup and VARI mass. The post warmup period was discretely (D) sampled $N = 1000$ times and also continuous (C) samples were recorded. The former 8 columns focus on the posterior random effects precision structure, where (unconditional) precisions are denoted by “Prec” and correlations by “corr”. The last two columns give the worst case time-weighted ESSes for the random- and fixed effects respectively. The best overall sampling efficiencies are indicated with **bold** font.

	rstan		pdphmc event spec. 1		pdphmc event spec. 3	
	post. mean	post. SD	post. mean	post. SD	post. mean	post. SD
μ_1	4.15	0.199	4.16	0.206	4.16	0.202
μ_2	4.12	0.263	4.12	0.244	4.12	0.268
μ_3	3.71	0.154	3.72	0.149	3.72	0.154
μ_4	4.11	0.095	4.11	0.092	4.11	0.092
μ_5	3.53	0.136	3.53	0.134	3.53	0.132
σ_1	0.31	0.009	0.31	0.009	0.31	0.009
σ_2	0.26	0.008	0.26	0.008	0.26	0.008
σ_3	0.29	0.009	0.29	0.009	0.29	0.009
σ_4	0.28	0.009	0.28	0.009	0.28	0.009
σ_5	0.25	0.009	0.25	0.009	0.25	0.009
δ_1	0.97	0.005	0.97	0.005	0.97	0.005
δ_2	0.98	0.004	0.98	0.004	0.98	0.004
δ_3	0.96	0.006	0.96	0.006	0.96	0.006
δ_4	0.94	0.008	0.94	0.008	0.94	0.008
δ_5	0.96	0.006	0.96	0.006	0.96	0.006
$\mathbf{H}_{2,1}$	0.39	0.003	0.39	0.003	0.39	0.003
$\mathbf{H}_{3,1}$	0.29	0.003	0.29	0.003	0.29	0.003
$\mathbf{H}_{4,1}$	0.29	0.003	0.29	0.003	0.29	0.003
$\mathbf{H}_{5,1}$	0.23	0.002	0.23	0.002	0.23	0.002
$\mathbf{H}_{3,2}$	0.20	0.003	0.20	0.003	0.20	0.003
$\mathbf{H}_{4,2}$	0.17	0.003	0.17	0.003	0.17	0.003
$\mathbf{H}_{5,2}$	0.12	0.002	0.12	0.002	0.12	0.002
$\mathbf{H}_{4,3}$	0.22	0.004	0.22	0.004	0.22	0.004
$\mathbf{H}_{5,3}$	0.18	0.003	0.18	0.003	0.18	0.003
$\mathbf{H}_{5,4}$	0.11	0.002	0.11	0.002	0.11	0.002
ν	33.61	0.291	33.61	0.289	33.61	0.278

Table 6: Posterior means and standard deviations for the parameters of the dynamic inverted Wishart model of Section 6. Only results based on discrete samples are presented for the pdphmc methods, as the continuous samples means are identical to the discrete samples means in the precision reported here.

E Dynamic inverted Wishart model details

The priors and transformations to a unrestricted domain for the parameters are given by

- $\delta_g \sim \text{iid } \text{Uniform}(-1, 1)$, $g = 1, \dots, G$. Sampling was performed in a scaled logit-transformed parameter.
- $\mu_g \sim \text{iid } N(0, 5^2)$, $g = 1, \dots, G$. No transformation applied.
- $\sigma_g^2 \sim \text{iid } p_0 s_0 / \chi_{p_0}^2$, $g = 1, \dots, G$, where $p_0 = 4$ and $s_0 = 0.25$. Sampling was performed in $\log(\sigma_g)$.
- $\mathbf{H}_{i,j} \sim \text{iid } N(0, 10^2)$, $j = 1, \dots, G - 1, i = j + 1, \dots, G$. No transformation applied.
- $\nu \sim \text{Uniform}(10.0, 60.0)$, Sampling was performed in a scaled logit-transformed parameter.

A fortunate property of this model, owing to the particular choice of observation equation (26) and scale matrix (27) is that $p(\mathbf{x}|\mathbf{Y}_{1:n}, \boldsymbol{\theta})$ factorizes as $\prod_{g=1}^G p(\mathbf{x}_{g,1:n}|\boldsymbol{\theta})h(\mathbf{x}_{g,1:n})$, i.e. the latent factors are conditionally on $\mathbf{Y}_{1:n}, \boldsymbol{\theta}$ independent over g . Moreover the function $h(\mathbf{x}_{g,1:n})$ has a particularly simple form

$$h(\mathbf{x}_{g,1:n}) \propto \prod_{k=1}^n \exp \left[\frac{\nu}{2} \mathbf{x}_{g,k} - \frac{\tilde{\mathbf{y}}_{g,k}}{2} \exp(\mathbf{x}_{g,k}) \right], \quad \tilde{\mathbf{y}}_{g,k} = [\mathbf{H}_{1:G,g}]^T \mathbf{Y}_k^{-1} [\mathbf{H}_{1:G,g}].$$

I.e. $p(\mathbf{x}|\mathbf{Y}_{1:n}, \boldsymbol{\theta})$ factorizes into the form of G independent (conditional on $\boldsymbol{\theta}$) smoothing distributions associated with single-dimensional state space models.

The transport map (see Osmundsen et al., 2021, for more details) $\gamma_{\boldsymbol{\theta}}$ relating \mathbf{x} and \mathbf{z} is given by

$$\mathbf{x}_{g,1:n} = \mathbf{h}_{g,\boldsymbol{\theta}} + \mathbf{L}_{g,\boldsymbol{\theta}}^{-T} \mathbf{z}_{(g-1)n+1:gn}, \quad g = 1, \dots, G$$

where $\mathbf{L}_{g,\boldsymbol{\theta}}$ is the lower Cholesky triangle of the SPD tri-diagonal matrix

$$\mathbf{G}_{g,\boldsymbol{\theta}} = \mathbf{G}_{g,\mathbf{x}|\boldsymbol{\theta}} + \mathbf{G}_{g,\mathbf{y}|\mathbf{x},\boldsymbol{\theta}}.$$

Here $\mathbf{G}_{g,\mathbf{x}|\boldsymbol{\theta}}$ is the (tri-diagonal) precision matrix of $\mathbf{x}_{g,1:n}|\boldsymbol{\theta}$ and $\mathbf{G}_{g,\mathbf{y}|\mathbf{x},\boldsymbol{\theta}}$ is the (diagonal) negative Hessian of $\mathbf{x}_{g,1:n} \mapsto \log(h(\mathbf{x}_{g,1:n}))$ evaluated at $\mathbf{h}_{g,\mathbf{y}|\mathbf{x},\boldsymbol{\theta}} = \arg \max_{\mathbf{x}_{g,1:n}} \log(h(\mathbf{x}_{g,1:n}))$ (this optimization problem splits into n separate single variable problems and is analytically solved). Finally

$$\mathbf{h}_{g,\boldsymbol{\theta}} = \mathbf{G}_{g,\boldsymbol{\theta}}^{-1} [\mathbf{G}_{g,\mathbf{x}|\boldsymbol{\theta}} E(\mathbf{x}_{g,1:n}|\boldsymbol{\theta}) + \mathbf{G}_{g,\mathbf{y}|\mathbf{x},\boldsymbol{\theta}} \mathbf{h}_{g,\mathbf{y}|\mathbf{x},\boldsymbol{\theta}}].$$

The Jacobian determinant of $\text{vec}(\gamma_{\boldsymbol{\theta}}(\mathbf{z}))$ reduces to $\prod_{g=1}^G |\mathbf{L}_{g,\boldsymbol{\theta}}^{-T}|$.

F Further work

A, by no means complete, list of possible further research directions related to NGRHMC processes contains the following:

- More adaptive event specifications in a similar vein to those of Hoffman and Gelman (2014); Betancourt (2016) to obtain trajectory lengths that are better adapted to local geometry of the target distribution. In this regard, working with multiple independent copies of target distribution, with negatively correlated momentums (across the copies) may be useful.
- The results of Section 3 goes through with minimal changes for non-Euclidian Riemann manifold Hamiltonian dynamics (Girolami and Calderhead, 2011) (see Appendix A.3). In this case, the dynamics solve

a coupled system of $2d$ first order ODEs (but cannot be reduced to a d -dimensional second order system). In particular, such a development could be carried out with explicit (non-symplectic) numerical integrators for first order systems, which could substantially reduce the often large computational cost of conventional Riemann manifold HMC (see e.g. Kleppe, 2018).

- Recently, pseudo-marginal/transport map MCMC methods (Alenlöv et al., 2016; Kleppe, 2019; Osmundsen et al., 2021) for large scale Bayesian hierarchical models have been proposed. Such methods result in a modified target distribution which “almost” factorizes into a low-dimensional general factor and a high-dimensional standard Gaussian factor. A symplectic integrator optimized for such a situation was developed in Alenlöv et al. (2016). A further development in this project would be to develop a non-symplectic integrator optimized for such “almost factorizing” situations, e.g., using splitting methods (see e.g. Franco and Gómez, 2014).
- It may be beneficial to operate with multiple event rates/momentum refreshes for different parts of the state vector. Theoretically, this should be rather straight forward, but finding good strategies for such a development would require substantial work.
- Reversible variants (based on involutions and reversible jump Metropolis Hastings) using the RKN methodology leads to approximate discrete time MCMC algorithms inheriting many of the properties of NGRHMC related to computational robustness. Such algorithms are attractive in that they allow very flexible adaptive selection of the Hamiltonian trajectory (time-)length distribution (e.g., similarly to NUTS). However, their efficient computation requires storing a representation of complete Hamiltonian trajectories and may involve simulation of substantial amounts of dynamics which is only used for calculating accept probabilities (both as opposed to the PDMP version).
- A further interesting property of NGRHMC processes is that biased (relative to the chosen momentum target distribution $N(\mathbf{0}_d, \mathbf{M})$) updates can be corrected by appropriately chosen event rates. This may be exploited e.g., toward higher momentums intended for jumps between modes, and implemented in a stable manner using the adaptive integrators.

G Simple R-implementation

The computations detailed in the paper are based on a rather complicated code written in C++ for best performance. The purpose of this section is to show that working implementations of NGRHMC processes for smaller problems or prototypes can also be implemented very easily in high level languages with access

to off-the-shelf (first order) ODE solvers. Below is an R-implementation of the proposed methodology based on the ODE code `lsodar` (from package `deSolve`) which supports root-finding/event capabilities. Such capabilities may be leveraged to run the whole simulation as single call to the solver.

The below code considers a zero mean bivariate target distribution with unit marginal variances and correlation 0.5. Other (bivariate) target distributions are obtained by simply changing the function `target.grad` accordingly. A constant $\lambda = 0.1$ and identity mass matrix \mathbf{M} was used. Since `lsodar` is a first order ODE code, the representation (2) of Hamilton's equations is used, and in addition Λ and continuous time temporal averages are added to the system of ODEs.

```

# Simple implementation of CTHMC based on the
# (first order ODE) solver lsodar provided by
# package "deSolve". The mass matrix is implicitly
# taken to be the identity, and a constant event rate
# is considered
set.seed(1)
# constants
lambda <- 0.1 # rather infrequent events
T <- 10000.0 # total simulation time
N.samples <- 2000 #How many uniformly spaced samples of the process

# consider a N(0,Sigma) target where
Sigma <- matrix(c(1,0.5,0.5,1),nrow=2)
prec <- solve(Sigma) # precision matrix
#target gradient (change to get another target distribution)
target.grad <- function(q){ return(-prec%*%q)}

# define the (first order ODE) for state
# state[1:2] : q
# state[3:4] : \dot{q} = p
# state[5] : \Lambda
# state[6] : u
# state[7:8] : \int q dt

ode <- function(t,state,parms){
  ret <- c(state[3:4], #\dot q = p
          target.grad(state[1:2]), # \dot p = gradient of log-target
          lambda, # \dot \Lambda = \lambda
          0.0, # u is constant
          state[1:2]) # integrated quantities
  return(list(ret)) #ODE solver assumes a list
}
#
# events occur when this function evaluate to 0: here \Lambda=u
#
root.fun <- function(t,state,parms){return(state[5]-state[6])}
#
# what happens at events?
#
at.event <- function(t,state,parms){
  newState <- c(state[1:2], # q unchanged
               rnorm(2), # p refreshed
               0.0, # reset Lambda
               rexp(1), # simulate new u
               state[7:8]) # continue integrating
  return(newState)
}

# initial state, starting from q=(1,1)
y0 <- c(1,1,# q(0)

```

```

    rnorm(2), #p(0)
    0.0, #Lambda
    rexp(1), #u
    0.0,0.0) #integrated quantities
#
# run actual simulation
#
sim.out <- deSolve::lsodar(y=y0,
                          func=ode,
                          times=seq(from=0,to=T,length.out = N.samples+1),
                          rootfunc = root.fun,
                          events = list(func=at.event,root=TRUE))

# display q_1 discrete samples
par(mfrow=c(1,2))
ts.plot(sim.out[, "1"])
acf(sim.out[, "1"])

# print summary stats
print(summary(sim.out[,c("1","2")]))
print(cor(sim.out[,c("1","2")]))

# construct integrated samples
eta.1 <- diff(sim.out[, "7"])*(N.samples/T)
# display integrated samples
ts.plot(eta.1)
acf(eta.1)
mean(eta.1) # estimator of E(q_1)
sd(eta.1) # < SD(q_1)

```
